Astronomy & Astrophysics

Models of turbulent dissipation regions in the diffuse interstellar medium

B. Godard[1], E. Falgarone[1], and G. Pineau des Forêts[2,1]

[1] LRA/LERMA, CNRS UMR 8112, École Normale Supérieure & Observatoire de Paris, Paris, France
e-mail: godard@lra.ens.fr
[2] Institut d'Astrophysique Spatiale, CNRS UMR 8617, Université Paris-Sud, Orsay, France

ABSTRACT

Aims. Supersonic turbulence is a large reservoir of suprathermal energy in the interstellar medium. Its dissipation, because it is intermittent in space and time, can deeply modify the chemistry of the gas. This is clearly seen in the framework of shock chemistry. Intense turbulent dissipation also occurs in regions of large velocity shears, sharing with shocks the property of intermittency. Whether these bursts of dissipation, short-lived and localized, have a measurable impact on molecular abundances in the diffuse medium, and how the chemical enrichment they drive compares to observations, are the questions we address here.

Methods. We further explore a hybrid method to compute the chemical and thermal evolution of a magnetized dissipative structure, under the energetic constraints provided by the observed properties of turbulence in the cold neutral medium. For the first time, we model a random line of sight by taking into account the relative duration of the bursts with respect to the thermal and chemical relaxation timescales of the gas. The key parameter is the turbulent rate of strain a due to the ambient turbulence. With the gas density, it controls the size of the dissipative structures, therefore the strength of the burst. It also sets the relative importance of viscous dissipation and ion-neutral friction in the gas heating and chemical enrichment.

Results. For a large range of rates of strain and densities, the models of turbulent dissipation regions (TDR) reproduce the CH$^+$ column densities observed in the diffuse medium and their correlation with highly excited H$_2$. They do so without producing an excess of CH. As a natural consequence, they reproduce the abundance ratios of HCO$^+$/OH and HCO$^+$/H$_2$O, and their dynamic range of about one order of magnitude observed in diffuse gas. Large C$_2$H and CO abundances, also related to those of HCO$^+$, are another outcome of the TDR models that compare well with observed values. Neutral carbon exceeds the abundance expected at ionization equilibrium, in agreement with fine-structure line observations. The abundances and column densities computed for CN, HCN and HNC are one order of magnitude above PDR model predictions, although still significantly smaller than observed values. The dependence of our results on the rate of strain and density reveals that the chemical enhancements are in better agreement with observations if the dissipation is dominated by ion-neutral friction, involving shear structures of thickness ~100 AU.

Key words. astrochemistry – turbulence – ISM: molecules – ISM: kinematics and dynamics – ISM: structure – ISM: clouds

1. Introduction

The diffuse medium has a major contribution to the mass of the interstellar medium (ISM) in galaxies like the Milky Way and as such is a key player in the star formation process. Although it is the first component of the ISM to have been discovered, and later on extensively analyzed through absorption measurements of atoms, ions and molecules (see the review of Snow & McCall 2006), its structure and properties remain a challenge in many respects:

(1) long thought to consist of two stable phases – the warm and cold neutral medium (WNM at temperatures $T \sim 8000$ K and CNM at $T \sim 100$ K) in thermal pressure equilibrium – a significant fraction of its emission is now detected at temperatures covering the whole range between those of the CNM and WNM (Heiles & Troland 2003);

(2) the CNM is turbulent with supersonic velocities, yet the velocity and density power spectra carry the signature of the Kolmogorov power spectrum for incompressible turbulence (Miville-Deschênes et al. 2003);

(3) its spatial and velocity structure is even a greater challenge since it has to reconcile the existence of structures observed at all scales in emission and a remarkable similarity of line profiles observed in absorption (see the discussion in Liszt & Lucas 1998 who question the elusive dimensionality of the diffuse medium). Since many tracers of the kinematics and small-scale structure of the diffuse ISM are molecular lines, clues are likely to be found in its surprisingly rich, but poorly understood, chemistry.

One major puzzle in this chemistry, raised by the detection of CH$^+$ in almost every line of sight sampling the CNM, persisted for decades because no formation path was found to be efficient enough in the diffuse ISM (Black et al. 1975; Black & Dalgarno 1977). It is rooted in the fact that in such diffuse gas, CH$^+$ forms via a highly endoenergetic reaction C$^+$ + H$_2$ ($\Delta E/k =$ 4640 K) unlikely to proceed at the low temperatures of the CNM. Similarly, one way to activate the oxygen chemistry in the diffuse medium, and therefore the formation of OH and H$_2$O, involves the reaction of O + H$_2$ which has an energy barrier of 2980 K.

A possibly related issue is the existence of rotationally excited H$_2$ in the diffuse gas. FUSE observations have revealed large populations in the $J > 2$ levels of H$_2$, inconsistent with fluorescence generated by the ambient UV field (Sonnentrucker et al. 2003; Gry et al. 2002; Nehmé et al. 2008a,b; Martin-Zaïdi et al. 2005; Lacour et al. 2005). This excited H$_2$ could be

localized in circumstellar material[1], but it also has been detected in the direction of late B stars, devoid of circumstellar matter, as in the data of Gry et al. (2002). Stellar UV photons are therefore unlikely to contribute significantly to the UV-pumping of H_2. In particular Lacour et al. (2005) find an increase of the Doppler parameter of the H_2 lines with J, supporting the existence of a warm component that cannot be heated by UV photons. They argue that this warm component cannot be due to H_2 formation pumping, as proposed by Sternberg & Dalgarno (1995) in dense PDRs, because it would require an H_2 formation rate larger than that inferred from observations, and would not reproduce the observed column densities of CH^+ found to correlate with excited H_2 (Spitzer et al. 1974; Snow 1976, 1977; Frisch & Jura 1980; Lambert & Danks 1986).

ISO-SWS observations further support the possible existence of a small fraction of warm gas in the Galactic diffuse medium by revealing its pure rotational line emission (Falgarone et al. 2005). Interestingly, the ratio $N(H_2)_{warm}/N_H \sim 2 \times 10^{-4}$, where $N(H_2)_{warm}$ is the H_2 column density in levels $J \geq 3$, is the same across the Galactic diffuse medium as in the direction of nearby late B stars. Recent *Spitzer* observations have confirmed the ISO-SWS line flux values (Verstraete et al., in preparation).

Both the observed abundances of CH^+ and column densities of rotationally excited H_2 suggest that large amounts of suprathermal energy are deposited in the cold diffuse medium. One obvious reservoir of suprathermal energy in the ISM is its turbulent kinetic energy. Attempts at incorporating this energy in the chemical networks of magneto-hydrodynamical (MHD) shocks have been partly successful at reproducing the observed properties of the diffuse medium (Pineau des Forêts et al. 1986; Draine & Katz 1986; Flower & Pineau des Forêts 1998). Other routes have been explored, involving dynamic interactions of the gas and the star cluster in the Pleiades (White 1984, 2003; Ritchey et al. 2006), turbulent transport between the WNM and CNM (Lesaffre et al. 2007) and turbulent dissipation taking place in regions of large velocity shears. Turbulence being intermittent in space and time (see the review of Anselmet et al. 2001), velocity shears may locally be large enough to drive large local heating rates and trigger the endoenergetic reactions of carbon and oxygen chemistries in the diffuse ISM (Falgarone et al. 1995). Along these lines, Joulain et al. (1998, hereafter J98) have explored the role of ion-neutral decoupling induced, in the weakly ionized diffuse medium, by the sharp gas accelerations in the regions of largest velocity-shear and its impact on ion-neutral chemistry, in particular the formation of CH^+ and HCO^+. Falgarone et al. (2006) have analysed the thermal and chemical relaxation phase in the evolution of a gas chemically enriched in a dissipation burst.

The observational data probing the molecular diversity and richness of the diffuse ISM are not restricted to CH^+ and HCO^+. In their long-lasting effort dedicated to unravelling molecular abundances in the diffuse ISM, Liszt & Lucas (2002, and references therein) have provided us with invaluable constraints. Not only did they show that the abundances of several molecules stay proportional to each other, with very well defined abundance ratios, but they found that the column densities of these molecules vary by more than one order of magnitude across clouds that all have about the same total hydrogen column density,

corresponding to diffuse and translucent clouds. They also revealed the remarkable similarity of HCO^+ and OH line profiles, all the more surprising for an ion and a neutral species, differently coupled to the magnetic field. On the contrary, the high-spectral resolution spectra of Crane et al. (1995) convincingly showed that the CH^+ line profiles are definitely broader and less Gaussian than those of CH, along the same lines of sight, while Lambert et al. (1990) found that, in the direction of ζ Oph, the CH line profiles could be seen as the sum of a broad component similar to the CH^+ profile, and a narrow one, close to that of the CN line. A similar result was obtained by Pan et al. (2004, 2005) towards stars of the CepOB2 and CepOB3 regions. These sets of results suggest that the velocity field is involved in the origin and the evolution of these molecules, and does so differently for each species.

It is therefore challenging to compare these available observations with models of a random line of sight across the diffuse ISM, where active dissipation bursts coexist with others in their relaxation phase. In particular, the possibility that a number of transient events may dominate the observed molecular column densities has never been addressed. This is what we do in the present paper. We restrict our study to densities lower than $n_H = 200$ cm^{-3} because, as will be seen, at higher densities and for the turbulent energy observed in the CNM, turbulent dissipation does not heat the gas enough to open the endoenergetic barriers mentioned above. We cannot rule out, though, rare dissipation bursts of exceptional intensity that would be able to heat still denser gas to the required temperature. We extend the previous studies in a way that allows us to explore the parameter domain, in particular those characterizing the ambient turbulence. We also extend the chemical network. We model a random line of sight across the diffuse medium and compare the predicted column densities of a variety of molecular species to the observations. The dynamic steady state is computed and described in Sect. 2, the chemistry in the active dissipation and relaxation phases is presented in Sects. 3 and 4. The modelling of a line of sight is discussed in Sect. 5. Comparisons of computed column densities with observations, as well as excitation diagrams of H_2, are shown in Sect. 6 and these results are discussed in Sect. 7.

2. Steady state of a magnetized vortex in a weakly-ionized diffuse gas

2.1. The neutral flow

Turbulence in the diffuse ISM is supersonic with respect to its cold phase, the CNM. Supersonic turbulence dissipates in shocks and regions of large velocity shear (Kritsuk et al. 2007). Their respective importance has been studied in numerical simulations. Porter et al. (1992, 1994) and Pavlovski et al. (2006) showed that most of the turbulent kinetic energy is rapidly transferred to high wavenumber non-compressible modes, once the shocks generated by supersonic turbulence have started to interact, reducing the role of compressible modes (shocks) in turbulent dissipation. In the so-called quiescent ISM (i.e. far from star forming regions), the smooth observed lineshapes support the view of a turbulence devoid of strong shocks (Falgarone et al. 1994) implying that the dissipation preferentially occurs in shear-layers.

Dissipative structures are modelled as shear-layers belonging to a solution of the Helmholtz equation for vorticity, close to the Burgers vortex adopted in J98: this analytical solution has the merit that it has only two free parameters that describe the balance between the stretching action of the large scales and the diffusion of vorticity across the vortex edge, at small scale. It

---

[1] Here, we deliberately overlook most of the early Copernicus results on H_2 high-J lines obtained in the direction of hot stars (e.g. Spitzer et al. 1973; Savage et al. 1977; Shull & Beckwith 1982) that led to the conclusion that excited H_2 absorption is occurring in circumstellar material heated/shocked by the star itself.

provides an analytical framework in which we can compute the effect of partial decoupling between ions and neutrals upon the steady state configuration of velocity and magnetic field and thus explore the effect of both the ion-neutral friction and viscous heating upon the chemical network.

The modified Burgers vortex is an axisymmetric solution elaborated in atmospheric sciences by Nolan & Farrell (1998). It is identical to the Burgers vortex at small radii r, in cylindrical coordinates (r, θ, z), and differs from it at large radii in the sense that the radial inflow velocity is not divergent at infinity:

$$u_r(r) = -\frac{a}{2} r \cdot e^{-\beta r^2} \tag{1}$$

where a is the turbulent rate of strain (in s^{-1}) and β (in cm^{-2}) describes the cut-off of the radial velocity. The axial velocity u_z, the vorticity ω_z and the orthoradial velocity u_θ are inferred from the Helmholtz and continuity equations:

$$u_z(r) = az \cdot e^{-\beta r^2} \cdot \left(1 - \beta r^2\right), \tag{2}$$

$$\omega_z(r) = \omega_0 \cdot e^{-\frac{a}{4\nu\beta}\left[1 - e^{-\beta r^2}\right]}, \tag{3}$$

$$u_\theta(r) = \frac{1}{r} \int_0^r r' \omega_z(r') dr' \tag{4}$$

where ω_0 is the peak of vorticity and ν is the kinematic viscosity. Any vortex is therefore entirely defined by three parameters, a, β and ω_0.

Note that, according to the radial dependence of the vorticity, the same equilibrium vortex radius r_0 as for the Burgers vortex can be defined,

$$r_0^2 = 4\nu/a \tag{5}$$

involving the two quantities that act on it, the rate of strain a and the viscosity ν. Accordingly, the vortex crossing time

$$\tau_c = \int_r^{kr} \frac{dr'}{u_r(r')} = \frac{2}{a} \ln(1/k) \tag{6}$$

for any constant $k < 1$ depends only on the rate of strain, while the vortex period, defined as

$$P = \frac{r_0}{u_\theta(r_0)} \tag{7}$$

depends on ν, a, and ω_0.

Because vorticity is radially non uniform there is a differential rotation of the fluid within the structure which induces a viscous dissipation rate:

$$\Gamma_{nn} = \sum_{i,j} \pi_{ij} \frac{\partial u_i}{\partial x_j} \tag{8}$$

where π_{ij} is the stress tensor. This rate is written in cylindrical coordinates:

$$\frac{\Gamma_{nn}}{\eta} = \left[\frac{\partial u_\theta}{\partial r} - \frac{u_\theta}{r}\right]^2 + \left(\frac{\partial u_z}{\partial r}\right)^2 + 2\left(\frac{\partial u_r}{\partial r}\right)^2 + 2\left(\frac{u_r}{r}\right)^2 + 2\left(\frac{\partial u_z}{\partial z}\right)^2 \tag{9}$$

where $\eta = \rho\nu$ is the dynamic viscosity in a gas of density ρ. It is computed for hydrogen atoms using the Kay & Laby (1966) tables of physical and chemical constants: $\eta = 6 \times 10^{-6} T_k^{1/2}$ g cm^{-1} s^{-1} where T_k is the gas kinetic temperature.

In all the following, it is assumed that the fluid description of the gas motions is justified because the mean free path

of H atoms $\lambda_{H-H} = 0.23(n_H/50 \text{ cm}^{-3})^{-1}$ AU in the diffuse medium, for a H-H elastic collision cross section[2] $\sigma_{H-H} = 5.7 \times 10^{-15}$ cm^2 (Spitzer 1978), is smaller than all the lengthscales involved in the model.

2.2. Interstellar constraints on the vortex parameters

As said above, each vortex is defined by a set of three independent parameters, a, β and ω_0. The cut-off parameter β has no influence either on the dynamics or on the chemistry of the structure as long as u_r is small compared to $u_{\theta,\max}$. Hereafter, β is chosen in order to satisfy this condition. In other words, turbulent dissipation in the vortex happens through radial vorticity distribution, not through a radial flux of matter. In these conditions, the dominant contribution to the viscous dissipation is the first term in Eq. (9).

Numerical simulations of incompressible turbulence (Jimenez 1997) and experiments (Belin et al. 1996) have shown that the maximum tangential velocity of filaments of vorticity $u_{\theta,\max} \sim \omega_0 r_0$ is of the order of the rms velocity dispersion of the ambient turbulence σ_{turb}. Since the equilibrium radius r_0 is set by the rate of strain a (Eq. (5)), ω_0 is also determined. In the case of interstellar turbulence, it implies that the orthoradial velocity in the vortex is supersonic with respect to the cold gas. It is noteworthy that slightly supersonic Burgers vortices have been found in experiments of rotating magnetized plasmas by Nagaoka et al. (2002) in conjunction with an inner density hole. Moreover, as will be seen later, the gas being violently and rapidly heated in the layers of largest orthoradial velocity, the Mach number there is likely to drop below unity. The only free parameter left in the vortex description is therefore the rate of strain a, although the gas density is in fact a free parameter that determines the vortex size, through the kinematic viscosity ν (Eq. (5)).

2.3. Magnetic field configuration and ionized flow

The configuration of the magnetic field and ions reached once the above vortex has developed in the partially ionized gas is numerically computed. The ions are *initially* at rest, threaded by a uniform magnetic field parallel to the z axis, $\boldsymbol{B}_0 = B_0 \boldsymbol{k}$. The ions are predominantly C$^+$, the neutrals are mainly composed of H and H$_2$ and the ionization degree, $x = 2 \times 10^{-4}$, is weak[3]. At $t = 0$, the ions are suddenly put into motion by friction with the vortex that developed in the neutral gas i.e. the three components of the neutral gas velocity $\boldsymbol{u}_n$ are those of the vortex given by Eqs. (1), (2) and (4). Boundary conditions are provided by the assumption that the vortex has a finite length L_V, apodised over a length C_V.

The alignment of ω with the ambient magnetic field is supported by the results of numerical simulations. Brandenburg et al. (1996) showed that in MHD turbulence, magnetic field and vorticity vectors tend to align with each other. More recently Mininni et al. (2006a,b) observed a similar behaviour in their 1536^3 numerical simulations.

Under these assumptions, we compute the two-dimensional time-dependent evolution of the ion velocity $\boldsymbol{u}_i$ and the magnetic field $\boldsymbol{B}$. We neglect the retro-action of the ions upon the

---

[2] For comparison the H$_2$-H$_2$ elastic collision cross section is $\sigma_{H_2-H_2} \sim 3 \times 10^{-15}$ cm^2 (Monchick et al. 1980).

[3] Computed for a diffuse molecular cloud of density $n_H \sim 50$ cm^{-3}, temperature $T_k \sim 100$ K, illuminated by the standard interstellar radiation field (ISRF).

Table 1. Parameters of the four models of Fig. 1. The density n_H and the turbulent rate of strain are fixed: $n_H = 50$ cm^{-3}, $a = 5 \times 10^{-10}$ s^{-1}.

			M_0	M_1	M_2	M_3
Magnetic field	B	μG	10	5	10	10
Vortex length	L_V	AU	200	200	100	200
Apodisation length	C_V	AU	100	100	50	50

neutral motions because, for densities in the range $10-200$ cm^{-3} and an ion-neutral drift velocity comparable to u_n (see Fig. 1), the friction force F_{in} they exert on the neutrals is negligible compared to the advection force in the vortical motion: $F_{in} \sim 10^{-3}(l/10 \text{ AU}) \times \rho_n u_n.\nabla u_n$, l being the spatial scale for the variation of u_n, in the range 10 to 100 AU. The neutrals velocity components are therefore those of the vortex (Eqs. (1), (2) and (4)) at any time.

In the interstellar medium $\boldsymbol{B}$ is frozen in the charged fluid (Spitzer 1978) and its evolution is simply written:

$$\frac{\partial \boldsymbol{B}}{\partial t} + \nabla \times (\boldsymbol{B} \times \boldsymbol{u}_i) = 0. \tag{10}$$

Neglecting the pressure gradients in the evolution equation of the ionized flow (this assumption is justified in Sect. 7) leads to:

$$\frac{\partial \boldsymbol{u}_i}{\partial t} + (\boldsymbol{u}_i \cdot \nabla)\,\boldsymbol{u}_i = \frac{\langle \sigma v \rangle_{in}}{(\mu_n + \mu_i)}\rho_n\,(\boldsymbol{u}_n - \boldsymbol{u}_i) + \frac{1}{4\pi\rho_i}\,(\nabla \times \boldsymbol{B}) \times \boldsymbol{B} \tag{11}$$

where μ_n and μ_i are the mean mass per particle of the neutrals (H, H$_2$) and ions (mostly C$^+$) respectively. $\langle \sigma v \rangle_{in} = 2.2 \times 10^{-9}$ cm^3 s^{-1} is the momentum transfer rate coefficient between the ionized and neutral fluids calculated by Flower & Pineau des Forêts (1995, Appendix A), and close to the Langevin rate.

We integrate Eqs. (10) and (11) by means of a two dimensional implicit scheme using the Alternating Direction Implicit method (*ADI*). To validate our approach we also use two other integration schemes: an explicit and an implicit without the *ADI* method. The results of our 300×200 points grid simulations are displayed in Fig. 1. Panel (a) shows the evolution of $|u_{i\perp}|_{max}$, the maximum ion velocity component perpendicular to the axis z, as a function of time. The curves correspond to the four models presented in Table 1. Panels (b) and (c) show the orthoradial and axial components of $\boldsymbol{B}$ for the model M_0 at $t = 100$ yr.

Figure 1a shows that the ions, initially at rest, are put into motion by the friction force from the neutrals in the vortex. This motion (including its boundary conditions) generates an orthoradial component B_θ of $\boldsymbol{B}$ and a gradient of B_z. These terms in turn induce magnetic tension and pressure gradient (see Eq. (10)), two forces resisting the orthoradial entrainment exerted by the neutrals. After ~ 100 yr, $|u_{i\perp}|_{max} < 0.4$ km s^{-1} which is small compared to $|u_{n\perp}|$ in the vortex (see Fig. 2 in Sect. 3.2) for all models. A steady state is reached in which the ions are almost back to rest and the magnetic field slightly helical (Fig. 1b). A large and steady state drift is set between the ion and neutral orthoradial velocities with an amplitude close to the orthoradial velocity of the neutrals in the vortex.

Such a drift has a deep impact on the chemistry of the gas, as was shown by J98, and contributes to the dissipation of its turbulent energy. The additional heating term due to the ion-neutral friction is written:

$$\Gamma_{in} = \frac{\rho_n\rho_i}{\mu_n + \mu_i}\,\langle \sigma v \rangle_{in}\,\frac{\mu_i}{\mu_n + \mu_i}\,(\boldsymbol{u}_i - \boldsymbol{u}_n)^2\,. \tag{12}$$
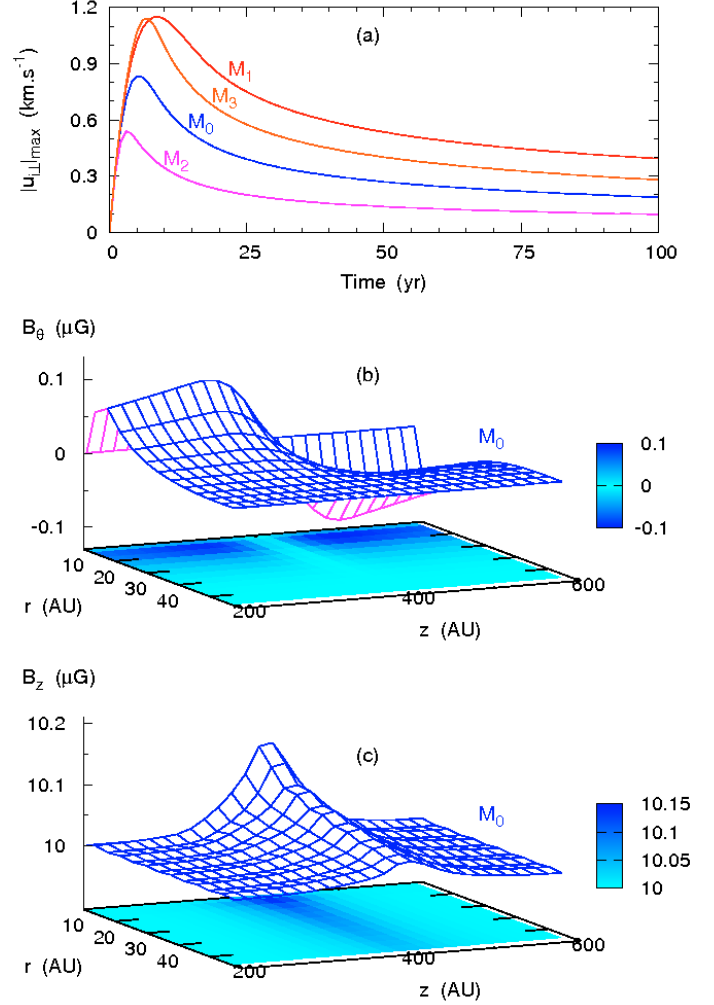

Fig. 1. Magnetic properties of the vortex. Panel **a)**: evolution of $|u_{i\perp}|_{max}$, the maximum ion velocity component perpendicular to the axis z, as a function of time. The different curves correspond to the models M_0, M_1, M_2 and M_3, (see Table 1). Panels **b)** and **c)**: orthoradial and axial components of the magnetic field at $t = 100$ yr for the model M_0 as functions of r and z.

We also found that there is only a very small ion-neutral drift in the z direction because the magnetic field is only slightly helical. Since in addition the contributions of the spatial variations of u_z to the heating term Γ_{nn} are negligible (Eq. (9)), we consider the vortex as invariant along the axis z and restrict our study of the spatial and time dependences to those occurring radially.

In the next sections we focus on the rapid thermal and chemical evolution of the gas trapped in such a steady state structure, and follow its thermal and chemical relaxation, once the vortex has blown-up.

3. The active phase

3.1. Numerical modelling

As in J98, we follow the Lagrangian evolution of a fluid particle trapped in the steady state vortex configuration. Because the vortex crossing time τ_c (see Sect. 2.1) is comparable to the chemical timescales, we compute non-equilibrium chemistry coupled to the time-dependent thermal evolution. The initial gas temperatures and molecular abundances are those of a steady state diffuse cloud of density n_H, illuminated by the ambient interstellar
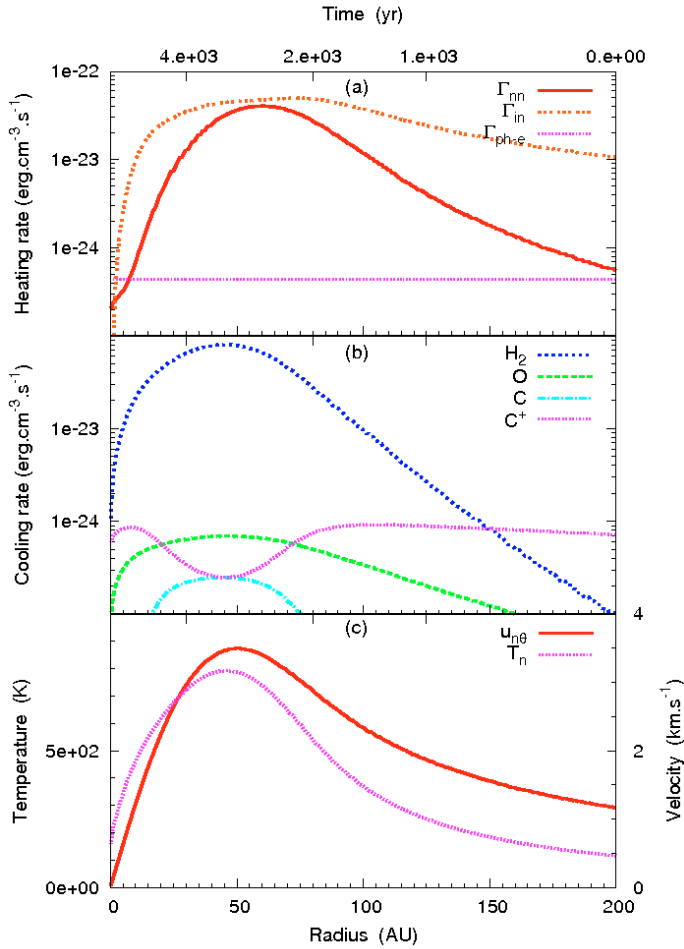
Fig. 2. Vortex physical properties as functions of the radius (bottom axis) or time (top axis, arbitrary origin) for the reference model: $a = 3 \times 10^{-11}$ s^{-1}, $n_H = 30$ cm^{-3} and $A_V = 0.4$ mag. Panel **a)**: the heating terms Γ_{nn} due to the viscous dissipation, Γ_{in} due to the ion-neutral friction and Γ_{ph-e} due to the photoelectric effect. Panel **b)**: the dominant cooling terms due to the radiative desexcitation of H$_2$ (pure rotational lines), C, O and C$^+$ (fine-structure lines). Panel **c)**: the temperature and orthoradial velocity of the neutrals.

radiation field (ISRF) (Draine 1978) scaled by the factor χ, and shielded by the extinction A_V. The cosmic ray ionization rate ζ and the elemental abundances are given in Table 2.

The neutrals and the ions are treated separately[4] and a fluid particle is defined at each time by its position r, the neutral and ionized velocity fields $\boldsymbol{u}_n$ and $\boldsymbol{u}_i$, the mass densities ρ_n and ρ_i, the temperatures of the neutrals T_n and ions T_i, and the abundances $n(X)$ of each species. The system therefore comprises 11 dynamic time-dependent variables (r, n_i, n_n, ρ_i, ρ_n, T_i, T_n, u_{nr}, $u_{n\theta}$, u_{ir}, $u_{i\theta}$). Our chemical network originates from the Meudon PDR code (Le Petit et al. 2006). It incorporates 90 species interacting through 1524 reactions. Those include the formation of H$_2$ on dust, the photoprocesses and the processes induced by the cosmic rays. We also compute the time-dependent evolution of the populations of the 18 first ro-vibrational levels of H$_2$ (corresponding to $T_{ex} < 10^4$ K).

---

[4] The ions and the electrons are treated as a unique fluid at a temperature T_i because: (1) the ion-electron velocity drift induced by the magnetic field fluctuations in the model is ~1 cm s^{-1}, negligible compared to the thermal velocities; (2) the ion-electron temperature equipartition time is ~0.1 $(T/1000$ K$)^{3/2}(n_i/3 \times 10^{-3}$ cm$^{-3})^{-1}$ yr (Spitzer 1978), also negligible compared to the dynamic timescales.

Table 2. Physical conditions and elemental abundances of the gas in the TDR models.

Density	n_H	cm^{-3}	10–200	
Radiation field	χ		1	
Extinction	A_V	mag	0.1–1	
Cosmic ray ionization rate	ζ	s^{-1}	3×10^{-17}	a
Elemental abundances			[X] / [H]	
Helium	[He]		1.00×10^{-1}	
Carbon	[C]		1.38×10^{-4}	
Oxygen	[O]		3.02×10^{-4}	
Nitrogen	[N]		7.94×10^{-5}	
Sulfur	[S]		1.86×10^{-5}	
Iron	[Fe]		1.50×10^{-8}	

a – Dalgarno (2006).

The system of variables is therefore driven by a set of 119 first-order coupled differential equations that are integrated along the fluid particle trajectory. To ensure that the time step is consistent with the variations of all dependent variables we use the DVODE differential equation solver (Brown et al. 1989).

The evolution of the thermal energy densities U_n and U_i is given by:

$$\frac{dU_n}{dt} = \frac{d}{dt}\left(\frac{3}{2}n_n k T_n\right) = B_n + \Gamma_{nn} + \Gamma_{in} + \Gamma_{en} \qquad (13)$$

$$\frac{dU_i}{dt} = \frac{d}{dt}\left(\frac{3}{2}n_i k T_i\right) = B_i + B_e + \frac{\mu_n}{\mu_i}\Gamma_{in} + \frac{\mu_n}{\mu_e}\Gamma_{en} \qquad (14)$$

where B_n, B_i and B_e are the sums of all the heating and cooling rates of the neutrals, the ions and the electrons respectively, not induced by turbulent dissipation, and Γ_{nn} and Γ_{in} the heating rates induced by turbulent dissipation defined in the previous section. Γ_{en} is the heating rate due to the electron-neutral drift, a term taken into account in the code but negligible compared to Γ_{nn} and Γ_{in}. The cooling rates include the radiative deexcitation of the ro-vibrational levels of H$_2$, of the fine structure levels of C$^+$, C and O and of the rotational levels of H$_2$O, OH and CO.

Lastly, since ions and neutrals are decoupled, we use the approximation of Flower et al. (1985) for the calculation of the chemical rate coefficients. The cross-section of a 2-species reaction is integrated over a Maxwellian velocity distribution at an effective temperature

$$T_{eff} = \frac{m_1 T_2 + m_2 T_1}{m_1 + m_2} + \frac{1}{3k}\frac{m_1 m_2}{m_1 + m_2}u_D^2 \qquad (15)$$

where m_1, m_2, T_1 and T_2 are respectively the masses and the temperatures of the 2 reactants and u_D their relative drift velocity.

3.2. Thermal evolution of the gas

Figure 2 displays the main properties of a reference model where $a = 3 \times 10^{-11}$ s^{-1}, $n_H = 30$ cm^{-3} and $A_V = 0.4$ mag. The vortex has an equilibrium radius $r_0 = 38$ AU and generates an average turbulent heating rate, $\overline{\Gamma}_{turb} = 3.4 \times 10^{-23}$ erg cm^{-3} s^{-1} defined as:

$$\overline{\Gamma}_{turb} = 2/(Kr_0)^2 \int_0^{Kr_0} [\Gamma_{nn}(r) + \Gamma_{in}(r)]r \, dr. \qquad (16)$$

The integration domain extends to the radius Kr_0 where the turbulent heating has no significant influence on the gas temperature and chemistry ($K \sim 5$).

In the model presented here, the heating rate is dominated everywhere by ion-neutral friction (Fig. 2a). For higher values of the turbulent rate of strain a, r_0 decreases (see Sect. 5.3) and the importance of the viscous dissipation increases because $u_{n\theta}$ is fixed by the ambient turbulence.

The gas in the vortex never reaches thermal balance and the thermal inertia is visible by comparing Figs. 2a and c where the peak temperature of the fluid particle is reached a few hundred years after the peak of the heating rate. Emission in the pure rotational lines of H_2 is by far the dominant coolant in the layers where $T_n \gtrsim 200$ K (Fig. 2c) while the cooling rate due to the ionized carbon C^+ decreases in the warmest layers. This is due to the chemical evolution (see Sect. 3.3).

Last, some chemical clues are provided in Fig. 2c. The neutral-neutral reactions only depend on the temperature T_n while the ion-neutral reactions depend on the ion-neutral drift. In Eq. (15), the second term of the right hand side reaches 1000 K as $u_D \sim 3$ km s^{-1}, an effective temperature higher than the peak kinetic temperature in the vortex. A comparison of the shapes of the orthoradial velocity $u_{n\theta}$ and the neutral temperature T_n shows that the endo-energetic ion-neutral chemistry is activated earlier in the fluid particle evolution than the neutral-neutral chemistry. For each type of vortex, the relative importance of those two chemical regimes is different.

3.3. Chemical evolution of the gas

The chemical evolution of the gas during the vortex active phase is similar to that reported in J98, although the chemical network is updated and includes nitrogen- and sulfur-bearing molecules. The outline of this network is given in Appendix C where we display the main production and destruction routes of the molecules of interest (1) in the ambient diffuse medium ($n_H = 30$ cm^{-3} and $A_V = 0.4$ mag) and (2) in the vortex for the reference model at a radius $r = r_0$.

The most important reaction route opened by the dissipative structure is the endothermic hydrogenation of C^+:

$$C^+ + H_2 \rightarrow CH^+ + H \qquad -\Delta E/k = 4640 \text{ K}. \qquad (17)$$
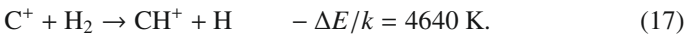
Besides the direct production of CH^+, this reaction is responsible for most of the chemical richness of the vortex as shown in Fig. C.2 (Appendix C): it enhances the production of CH_3^+ via the successive hydrogenation by H_2 of CH^+ and CH_2^+. CH_3^+, in turn, enhances the production of molecules including CH and C via the dissociative recombination with electrons, HCO^+ and CO via
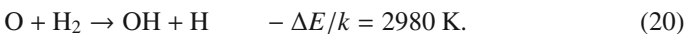
$$CH_3^+ + O \rightarrow HCO^+ + H_2 \qquad (18)$$

and CN, HCN and HNC via

$$CH_3^+ + N \rightarrow HCN^+ + H_2. \qquad (19)$$

The production of CH_3^+ is also at the origin of C_2H and CS since these molecules are both products of CH (through the reactions $CH + C^+ \rightarrow C_2^+ + H$ and $CH + S^+ \rightarrow CS^+ + H$ respectively).

The second main reaction, absent in the ambient medium, which plays an important role in the chemical evolution of the vortex is:

$$O + H_2 \rightarrow OH + H \qquad -\Delta E/k = 2980 \text{ K}. \qquad (20)$$

Besides the direct production of OH it triggers the production of H_2O via

$$OH + H_2 \rightarrow H_2O + H \qquad -\Delta E/k = 1490 \text{ K} \qquad (21)$$
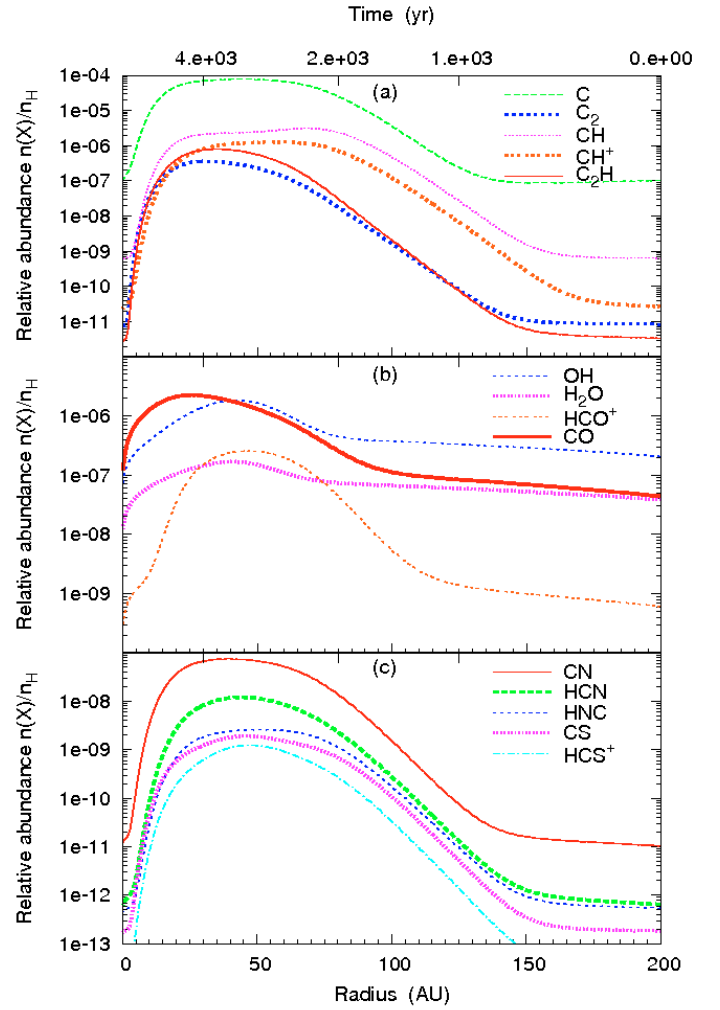

Fig. 3. Fractional abundances relative to $n_H = n(H) + 2n(H_2)$ of selected species as functions of the radius (bottom axis) or time (top axis, arbitrary origin) for the reference model: $a = 3 \times 10^{-11}$ s^{-1}, $n_H = 30$ cm^{-3} and $A_V = 0.4$ mag.

and O_2 via

$$OH + O \rightarrow O_2 + H. \qquad (22)$$

Figure 3 displays the evolution of several relative abundances in the magnetized vortex. The impact of the turbulent heating is such that most species abundances rise from 2 to 5 orders of magnitude within the structure. The formation of vortices in the turbulent gas flow therefore has specific chemical signatures that we expect to observe in the diffuse medium. One remarkable example is HCO^+. Since this molecule is a direct product of CH_3^+ (in the vortex) it becomes related to almost all the species whose abundance is enhanced in the vortex.

Time (and space) stratification is also visible in Fig. 3: the chemical enrichments occur successively, because the ion-neutral chemistry is triggered earlier than the neutral-neutral chemistry (see previous section) and because the chemical inertia of each species is different.

4. The relaxation phase

4.1. Numerical modelling

Once the burst of turbulent dissipation is over, some chemical signatures imprinted in the gas persist for several thousand years
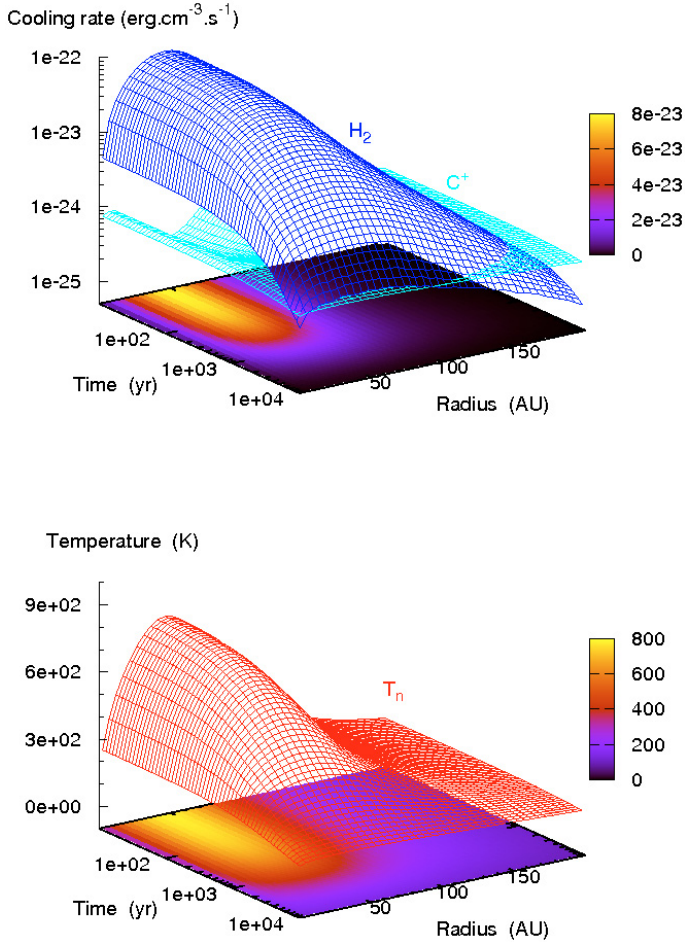
Fig. 4. Vortex thermal features during the relaxation phase, as functions of the radius and time (after the vortex blow-up) for the reference model: $a = 3 \times 10^{-11}$ s^{-1}, $n_H = 30$ cm^{-3} and $A_V = 0.4$ mag. An isochoric relaxation is assumed. *Top panel*: the main cooling terms, i.e. the radiative desexcitation of H$_2$ and C$^+$. *Bottom panel*: the temperature of the neutrals.

Fig. 5. Column densities of selected species, integrated across the reference vortex, as functions of time during an isochoric relaxation phase.

as shown by Falgarone et al. (2006). To compute the chemical and thermal relaxation of the gas, we assume that, once the vortex has vanished, the gas is dynamically frozen: $\boldsymbol{u} = 0$. The previous Lagrangian approach is switched to Eulerian, and we compute the time-dependent evolution of each cell in the vortex. The initial conditions of the relaxation are the conditions of the active stage at every position. The thermal Eqs. (13) and (14) are still valid with $\Gamma_{nn} = 0$ and $\Gamma_{in} = 0$.

While the numerical code has been conceived to treat isobaric or isochoric relaxation, all the results presented in this paper were obtained assuming isochoric relaxation, because it allows us to better disentangle what is due to the chemistry itself from what is due to the gas density. In particular, it shows more clearly the role of the relaxation timescales of the molecules, i.e. only driven by the chemical network and the thermal evolution, independently of the gas density.

4.2. Thermal evolution of the gas

Figure 4 displays the main cooling rates (top panel) and gas temperature (bottom panel) as functions of time and position in the vortex (after the vortex blow-up). It shows that as in the active phase, the cooling rate during the relaxation phase is dominated by the emission in the pure rotational lines of H$_2$. In the model
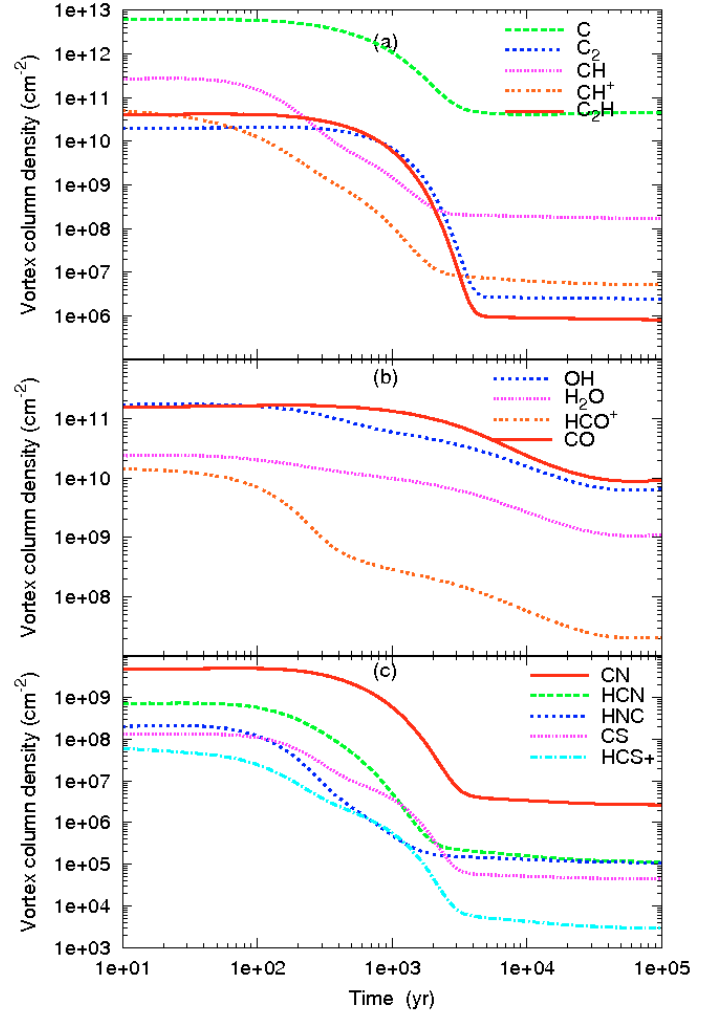
presented here ($n_H = 30$ cm^{-3}), other cooling agents (mainly C$^+$) become dominant at $t \sim 10^4$ yr.

4.3. Chemical evolution of the gas

During relaxation, the cooling of the gas causes all the endo-energetic reactions triggered during the dissipative burst to slow down and stop, one after the other. The gas loses its chemical enrichment at a speed that depends on the molecular species. This is illustrated in Fig. 5 that displays the time-dependent evolution of the column density $N_{VR}(X, t)$ of selected species X integrated across the vortex.

For most species (CO, C$_2$, OH, H$_2$O, C$_2$H ...) the signature of the turbulent dissipation persists over more than 10^3 yr. The characteristic timescales (e-folding times) differ between species by more than a factor of 30 ($\approx 2 \times 10^2$ yr for CH$^+$ and 7×10^3 yr for CO). The existence of the relaxation phases modifies the correlations between molecular abundances. One example is provided by HCN and C$_2$H that follow a similar enhancement in the active phase (see Fig. 3) and have markedly different behaviours in the relaxation phase.

The richest phases are not necessarily those contributing the most to the observable column densities because they have short lifetimes. In the next section, we detail how we take

time-variability into account in our modelling of a random line of sight across the diffuse medium.

5. Modelling of a line of sight

In turbulent flows, the spatial distribution of the regions of highest dissipation rate (extrema of velocity shear, extrema of negative velocity divergence i.e. shocks) is far from space-filling, one of the aspects of the intermittent nature of turbulence. The filling factor of these extrema has been computed in numerical simulations of mildly compressible (Pety & Falgarone 2000) or supersonic MHD turbulence (Pavlovski et al. 2006; Pan & Padoan 2008). Moisy & Jimenez (2004) have shown that the regions of intense vorticity tend to form filaments, while regions of most intense dissipation rather form sheets or ribbons, all of them being organized in clusters, probing the organization of small-scale intermittent structures.

For our purpose, we assume that any line of sight intercepts a number of vortices, either active or in their relaxation phase. The total number of vortices per line of sight is constrained by the average transfer rate of turbulent energy per unit volume available in the cascade.

5.1. Method

Any line of sight samples three kinds of diffuse gas: (1) the ambient medium in which the chemistry is computed as steady state UV-dominated chemistry; (2) a number $\mathcal{N}_{VA}$ of active vortices and (3) a number of relaxation phases related to $\mathcal{N}_{VA}$. We also consider that the line of sight is homogeneous and characterized by its density n_H and uniform shielding A_V from the ISRF. Such an approximation is useful to test the importance of each parameter (a, n_H and A_V) on the final chemical state of the gas. Last, we assume that all the vortices in the line of sight are identical: they all have the same turbulent rate of strain a. In the following section we show why a more realistic description, with a distribution of rate of strain values, would not provide very different results, namely because, as it will be seen, the results depend weakly on a.

The contribution of one active phase of duration τ_V to the total column density of a species X is $N_{VA}(X)$. The contribution of the relaxation phase of that species is computed by assuming that the longer its relaxation timescale, the greater the contribution of the relaxation phase in the observed column density so that the chemical composition of a line of sight is entirely determined by the number of active vortices $\mathcal{N}_{VA}$ and their lifetime τ_V. The resulting column density of a species X is:

$$N(X) = \mathcal{N}_{VA}(X) \left[N_{VA}(X) + 1/\tau_V \int_0^\infty N_{VR}(X,t)\mathrm{d}t \right] + N_M(X) \quad (23)$$

where $N_M(X)$ is the contribution of the ambient medium.

5.2. Constraints provided by the energy available in the turbulent cascade

5.2.1. The number of active vortices

The number of active vortices $\mathcal{N}_{VA}$ in a line of sight and their lifetime τ_V, are constrained by the turbulent energy available in the cascade and its transfer rate. In turbulent flows, the transfer rate of kinetic energy at scale l of characteristic velocity u_l is, on average:

$$\varepsilon_l = \frac{1}{2}\rho \frac{u_l^3}{l}. \quad (24)$$

The Kolmogorov scaling of turbulence, valid for incompressible turbulence, postulates that this transfer rate is scale-independent. In the highly compressible interstellar medium, one would expect this quantity to differ from one scale to another. Measurements of the internal velocity dispersion of clouds of size l combined with their density provide an estimate of the turbulent energy transfer rate at this scale. A compilation of CO(1–0) line observations of interstellar structures of size ranging between 10^{-2} and 10^3 pc shows that ε_l is remarkably independent of the scale in the Galaxy and that there is a large scatter (by a factor of 100) about a well defined average value $\overline{\varepsilon}_{obs} \sim 2 \times 10^{-25}$ erg cm^{-3} s^{-1} (Falgarone 1998; Hily-Blant et al. 2008). A similar value holds for turbulence in the HI CNM and in non-star-forming dense cores (Falgarone 1999). The uniformity of this value across the local ISM suggests that the turbulent cascade encompasses the different regions of the cold medium, and that the transfer is driven by turbulence at the same rate, in all media, whatever the gas density.

We adopt the above value of $\overline{\varepsilon}_{obs}$ in our model as representative of the turbulent energy transfer rate through scales. We thus impose that, at any time, the dissipation rate in all the active vortices in a line of sight is equal to the average energy transfer rate in the turbulent cascade, so that:

$$\overline{\varepsilon}_{obs} = \mathcal{N}_{VA}\overline{\Gamma}_{turb} 2Kr_0/L \quad (25)$$

where L is the depth of the line of sight, inferred from $L = N_H/n_H$. This fixes the number of active vortices in a given line of sight[5]. This number and many of the results are therefore proportional to $\overline{\varepsilon}_{obs}$.

5.2.2. The velocity dispersion of the ambient turbulence

The energy transfer rate depends on the density, velocity dispersion and timescale. We thus need to know the amount of turbulent energy available in the CNM component of the diffuse medium, or the rms turbulent velocity in the CNM. It is this quantity that sets the angular velocity of the vortex (see Sect. 2.2). This quantity is difficult to determine on observational grounds, because of the mixture of WNM and CNM in the HI emission spectra and because of the lack of spatial information for the absorption spectra (dominated by the CNM). We adopt a rms velocity dispersion $\sigma_{turb} = 3.5$ km s^{-1} for the CNM turbulence derived from the HI maps of a high latitude cirrus in the Polaris Flare (Joncas et al. 1992; Miville-Deschênes et al. 2003) in which HI emission is well correlated with the 100 μm emission of dust, probing column densities of gas representative of the CNM. This value is consistent with those quoted in Crovisier (1981) for the CNM. It is comparable to the geometric mean of the two smallest values, $FWHM = 4.9$ and 12.0 km s^{-1} inferred by Haud & Kalberla (2007) from the Gaussian decomposition of the HI profiles of the Leiden/Argentine/Bonn survey of galactic HI (Hartmann & Burton 1997). Last, this rms velocity dispersion is consistent with the approximate equipartition between magnetic and turbulent energy inferred by Heiles & Troland (2005) from the median value of the magnetic field estimated in the diffuse medium $B = 6$ μG.

---

[5] $\mathcal{N}_{VA}$ also depends on the angle of inclination of the vortices along the line of sight. Because the dynamics and the chemistry in a vortex do not depend on the axial coordinates z and because the model is axisymmetric, this angle has no influence on the final results. $\mathcal{N}_{VA}$ is thus defined for vortices perpendicular to the line of sight.
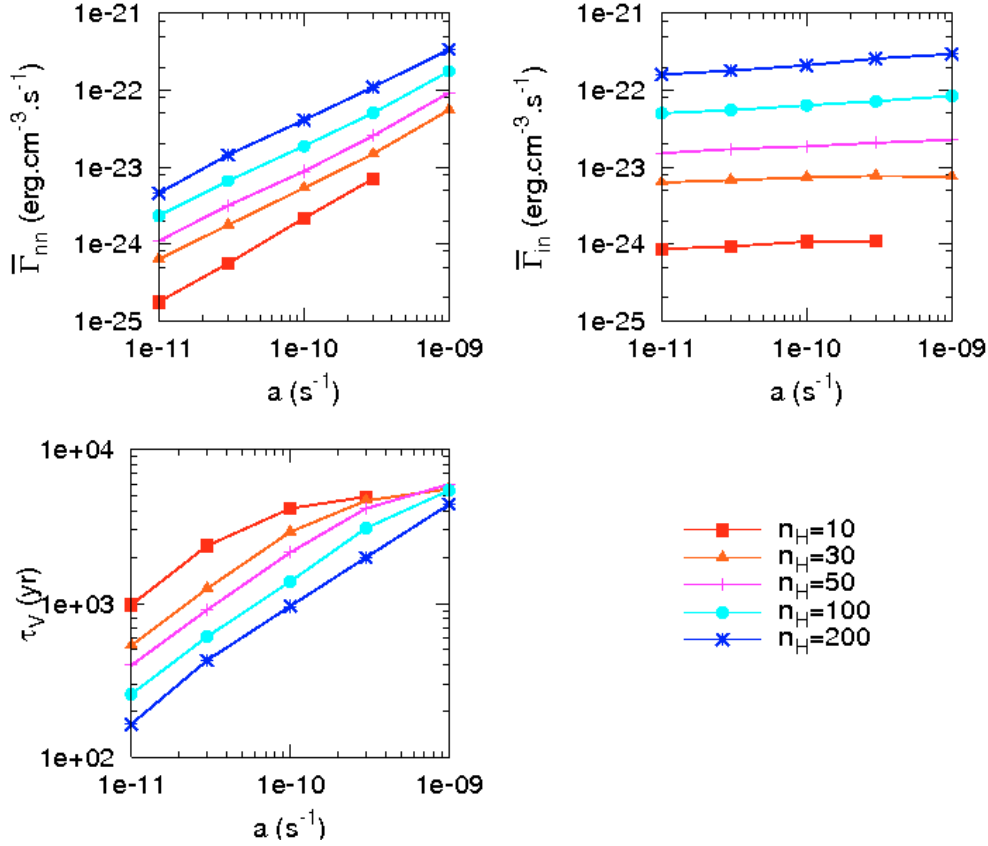
Fig. 6. Main physical properties of the TDR models as functions of the turbulent rate of strain a for several values of the density n_H. *Top panels*: the vortex heating terms $\overline{\Gamma}_{nn}$ due to the viscous dissipation (*left*) and $\overline{\Gamma}_{in}$ due to the ion-neutral friction (*right*). *Bottom panel*: the vortex lifetime τ_V.

5.2.3. The lifetime of the active phase

The lifetime of an active vortex, τ_V, is controlled by the large-scale motions of the ambient turbulence that feed energy into the small-scale structures (Moffatt et al. 1994). It may exceed the period of the vortex as suggested by a variety of experiments in incompressible turbulence (e.g. Douady et al. 1991). This lifetime is uncertain, though, and its value in our model is constrained by energetic considerations.

We assume that, for simplicity, all the vortices explored in the models dissipate the same total energy over their lifetime τ_V

$$E = \pi (Kr_0)^2 \, \overline{\Gamma}_{turb} \, L_V \, \tau_V. \qquad (26)$$

This constraint fixes the lifetime τ_V of the vortex i.e. the time during which turbulent dissipation is active. In order to stay in the vortex framework we impose that τ_V is larger than the vortex period P, which sets a lower limit to E. The influence of this parameter on the results is discussed in Appendix B.

5.3. The role of the rate of strain and density under the energetic constraints

Once $\overline{\varepsilon}_{obs}$, σ_{turb} and E are given, a line of sight is therefore defined by only three independent parameters: the turbulent rate of strain a, the gas density n_H and the shielding A_V.

To help the reader understand the chemical results presented in the next section, we discuss the roles of the rate of strain and gas density because the above constraints on the energy dissipation rate actually couple a and n_H that should be independent parameters. This is so because the two energy constraints (transfer rate and energy) involve the equilibrium radius r_0 that primarily

depends on a but also on n_H, via the density dependence of the kinematic viscosity (see Sect. 2.1). These trends are illustrated in Figs. 6 and 7 that also display the dependence of several key quantities on a and n_H.

Figure 6 shows that, as expected, $\Gamma_{nn} \sim a n_H$ is almost proportional to a because the higher the rate of strain, the smaller the equilibrium radius and the larger the velocity shear. Γ_{in} is almost independent of a and increases with density as $\Gamma_{in} \propto u_D n_H^2$ so that, depending on a and n_H, two regimes exist: one at low density and high rate of strain where the turbulent heating is dominated by viscous dissipation, and the other (small a, high density) where this heating is dominated by the ion-neutral friction. The rate of strain a therefore plays an important role in the nature of the warm chemistry triggered in the vortex. This figure also displays the run of τ_V with the rate of strain for different densities, as a result of the constraint on the total energy E dissipated in each vortex.

Figure 7 shows that r_0 is small in the former regime and reaches values of the order of 100 AU in the regime where ion-neutral friction dominates. The peak gas temperature reached in the vortex, T_{max}, is also shown: it is higher in the regime where viscous dissipation dominates because the orthoradial velocity is fixed and thin vortices induce large velocity shears, thus large viscous heating. However, the thermal inertia of the gas prevents it from reaching much higher temperatures, because the most efficient vortices (large a) are short-lived. The range of a and n_H explored in our study covers these two regimes and we quantify the chemical effects of turbulent dissipation as it changes from dominated by ion-neutral friction to dominated by viscous dissipation.
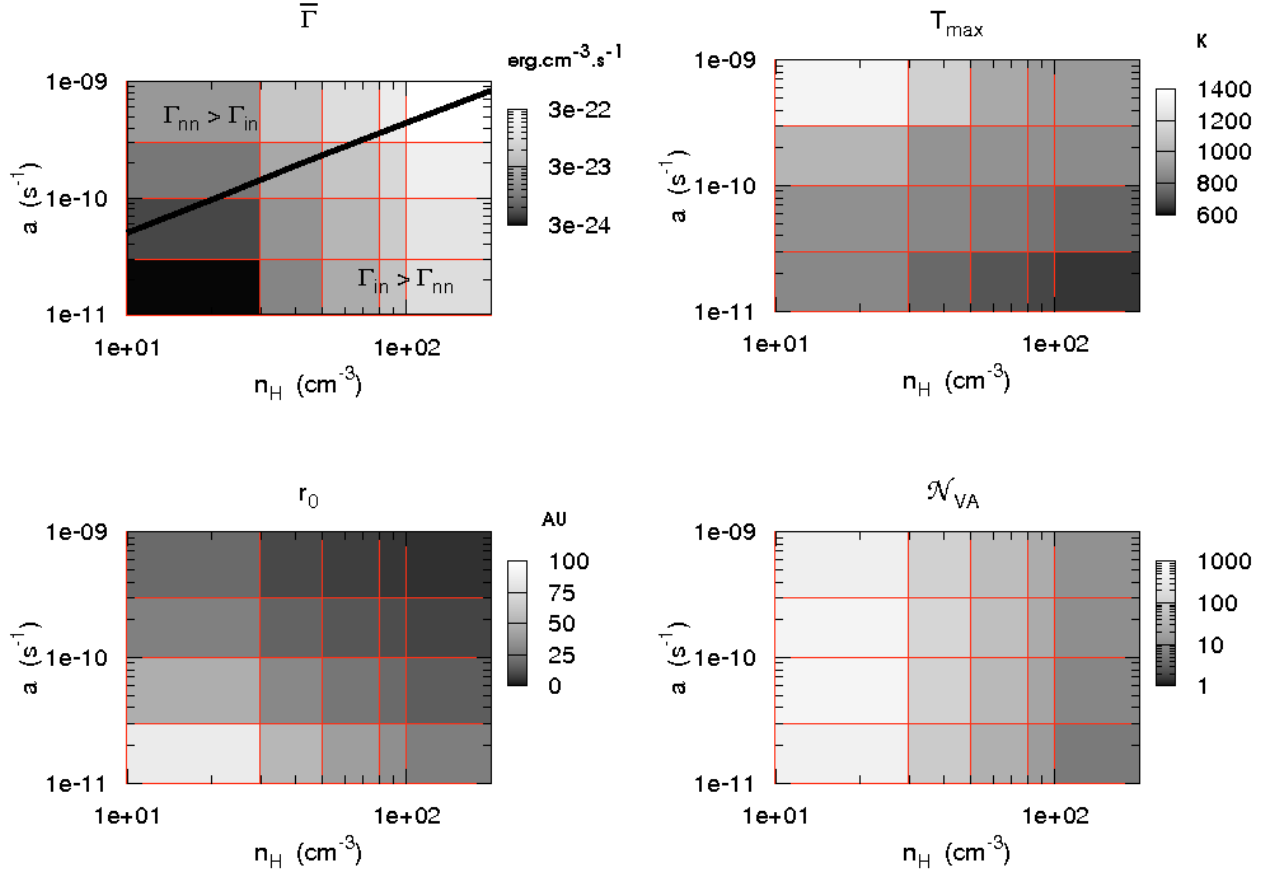
Fig. 7. Main physical properties of the TDR models as functions of the turbulent rate of strain a and of the density n_H of the gas. *Top panels*: the vortex turbulent heating rate $\overline{\Gamma}_{turb}$ (*left*) and the vortex maximum temperature T_{max} (*right*). *Bottom panels*: the vortex radius r_0 (*left*) and the number of active vortices $\mathcal{N}_{VA}$ along a line of sight sampling one magnitude of gas (*right*).

Last, we find that the number of active vortices $\mathcal{N}_{VA}$ (computed for a line of sight sampling one magnitude of gas) is roughly independent of a and decreases almost as n_H^{-2} as the density increases. This is because $\overline{\varepsilon}_{obs}$ is fixed (see previous section), and because of the combined dependences of r_0, $\overline{\Gamma}_{turb}$ and L on a and n_H (see Eq. (25)). We note that $\mathcal{N}_{VA}$ reaches large values at low density (up to several hundreds along lines of sight of several tens of parsecs). However the filling factor of the vortices

$$f_v = \mathcal{N}_{VA} \frac{2Kr_0}{L} \qquad (27)$$

never exceeds $f_v = 4 \times 10^{-2}$, its lowest values being $f_v \sim 10^{-4}$ at high densities and rates of strain.

5.4. The respective contribution of each chemical regime

Three different chemical regimes enter our line of sight modelling, associated with the active phase, the relaxation phase and the ambient medium. Their respective contributions to the integrated column density of a species X (see Eq. (23)),

$$f_M(X) = N_M(X)/N(X) \qquad (28)$$

$$f_{VA}(X) = \mathcal{N}_{VA}(X)N_{VA}(X)/N(X) \qquad (29)$$

$$f_{VR}(X) = \mathcal{N}_{VA}(X) \int_0^\infty N_{VR}(X,t)\mathrm{d}t/N(X)\tau_V \qquad (30)$$

depend on this species and are given in Tables 3 and 4.

For numerical reasons the contributions $f_{VA}(X)$ and $f_{VR}(X)$ are computed as excesses of the density $n(X)$ in the active and relaxation phases respectively, above its value in the ambient medium. Hence $N_M(X) = f_M(X) \times N(X)$ is the column density of the species X along a line of sight without vortices of total column density $N_H = 1.8 \times 10^{21}$ cm^{-2}.

Tables 3 and 4 show that all the regimes have a significant contribution, although most of the selected species are predominantly formed in the vortices.

6. Results: comparison with the observations

We have computed 150 different models exploring the parameter space as follows:

- 6 densities ($n_H = 10, 30, 50, 80, 100, 200$ cm^{-3});
- 5 rates of strain ($a = 1, 3, 10, 30, 100 \times 10^{-11}$ s^{-1});
- 5 UV shieldings ($A_V = 0.2, 0.4, 0.6, 0.8, 1$).

The turbulent rate of strain extends over two orders of magnitude, the largest value corresponding to the condition $r_0 \gg \lambda_{HH}$ for all densities, the smallest being the limit of validity of our analytical approach.

In this section, we present the results of our line of sight models (named Turbulent Dissipation Regions models or TDR models) on the same displays as large sets of observational data. We also compare these data with results obtained from PDR models (two-side illuminated slabs of uniform density, Meudon PDR code, Le Petit et al. 2006), computed with the

Table 3. Physical and chemical characteristics of two TDR-models defined by their parameters n_H, A_V and a. $f_M(X)$, $f_{VA}(X)$ and $f_{VR}(X)$ are the contributions of the ambient medium, the active and the relaxation phases respectively, to the column density $N(X)$ of the species X. All models are computed for $N_H = 1.8 \times 10^{21}$ cm^{-2}. The relative abundances are given in the last columns. Numbers in parenthesis are powers of 10.

	Parameters								
n_H		30 cm^{-3}					100 cm^{-3}		
A_V		0.1 mag					0.1 mag		
a		3 ($-$11) s^{-1}					3 ($-$11) s^{-1}		
	Physical properties								
$\overline{\Gamma}_{turb}$		9.3 ($-$24) erg cm^{-3} s^{-1}					6.9 ($-$23) erg cm^{-3} s^{-1}		
T_{amb}		114 K					58 K		
T_{max}		1000 K					807 K		
τ_V		1070 yr					506 yr		
r_0		40 AU					21 AU		
$\mathcal{N}_{VA}$		215					17		
f_v		2.2 ($-$2)					2.9 ($-$3)		
	Chemical properties								
Species	$f_M(X)$ %	$f_{VA}(X)$ %	$f_{VR}(X)$ %	$N(X)$ cm^{-2}	$N(X)/N_H$	$f_M(X)$ %	$f_{VA}(X)$ %	$f_{VR}(X)$ %	$N(X)$ cm^{-2}	$N(X)/N_H$
---	---	---	---	---	---	---	---	---	---	---
H	100	0[a]	0[a]	7.0 (20)	3.9 ($-$01)	100	0[a]	0[a]	2.8 (20)	1.6 ($-$02)
H$_2$	100	0[a]	0[a]	5.5 (20)	3.1 ($-$01)	100	0[a]	0[a]	7.6 (20)	4.2 ($-$01)
H$_3^+$	81	5	14	2.9 (13)	1.6 ($-$08)	93	2	5	1.2 (13)	6.7 ($-$09)
C	19	65	35	4.4 (14)	2.4 ($-$07)	68	23	9	5.6 (14)	3.1 ($-$07)
CH	5	86	9	8.1 (12)	4.5 ($-$09)	22	69	9	7.9 (12)	4.4 ($-$09)
CH$^+$	0.2	96	4	2.2 (13)	1.2 ($-$08)	2	95	3	1.3 (12)	7.2 ($-$10)
C$_2$	0.5	72	28	4.0 (11)	2.2 ($-$10)	3	46	51	1.4 (12)	7.8 ($-$10)
C$_2$H	0.1	76	24	6.3 (11)	3.5 ($-$10)	0.4	61	39	3.5 (12)	1.9 ($-$09)
OH	52	17	31	8.7 (13)	4.8 ($-$08)	63	18	19	2.3 (13)	1.3 ($-$08)
H$_2$O	57	11	32	1.3 (13)	7.2 ($-$09)	68	14	18	3.6 (12)	2.0 ($-$09)
H$_3$O$^+$	35	23	42	1.3 (13)	7.2 ($-$09)	32	40	28	1.1 (12)	6.1 ($-$10)
CO	57	16	27	2.6 (13)	1.4 ($-$08)	67	12	21	3.0 (13)	1.7 ($-$08)
HCO$^+$	14	69	17	8.4 (11)	4.7 ($-$10)	11	77	12	3.7 (11)	2.1 ($-$10)
O$_2$	67	11	22	3.8 (10)	2.1 ($-$11)	80	10	10	4.1 (10)	2.3 ($-$11)
SH$^+$	0.1	98	2	6.2 (11)	3.4 ($-$10)	0.2	98	2	2.1 (11)	1.2 ($-$10)
CS	3	85	12	1.8 (09)	1.0 ($-$12)	11	69	20	7.0 (09)	3.9 ($-$12)
HCS$^+$	0.6	93	7	1.1 (09)	6.1 ($-$13)	1	89	10	1.9 (09)	1.1 ($-$12)
CN	1	79	20	2.3 (11)	1.3 ($-$10)	8	63	29	1.6 (11)	8.9 ($-$11)
HCN	0.5	88	12	3.3 (10)	1.8 ($-$11)	3	81	16	2.6 (10)	1.4 ($-$11)
HNC	2	89	9	5.9 (09)	3.3 ($-$12)	17	74	9	4.0 (09)	2.2 ($-$13)

[a] For the reason given in Sect. 5.4 $f_{VA}(H) = f_{VR}(H) = f_{VA}(H_2) = f_{VR}(H_2) = 0$, because the densities of H and H$_2$ are not modified in the vortex.

same conditions as in the TDR models: $\chi = 1$, $\zeta = 3 \times 10^{-17}$ s^{-1} and with the same chemical network.

The amount of gas along the line of sight in the PDR and TDR models is normalized to $N_H = 1.8 \times 10^{21}$ cm^{-2} because, as will be shown later, it corresponds to most of the data collected in the visible, UV and radio ranges.

6.1. Ultraviolet and visible observations towards nearby stars

An important clue for the understanding of the diffuse ISM chemistry is provided by the combined observations of CH and CH$^+$ (Gredel et al. 1993; Crane et al. 1995; Gredel 1997; Pan et al. 2004, 2005; Sheffer et al. 2008). Although CH$^+$ is known to be overabundant, the column densities of CH are in agreement with the predictions of the PDR models. Because the two species are tightly related by the chemistry (see Figs. C.1 and C.2 in Appendix C), the difficulty of any modelling is then to understand the physics which leads to an enhancement of CH$^+$ without changing the amount of CH. Another important clue lies in the correlation, mentioned in the Introduction, between CH$^+$ and the pure rotational $J \geqslant 3$ levels of H$_2$.

The CH$^+$, CH and excited H$_2$ observational data are displayed in Fig. 8 with the prediction of several PDR models (left panels) and TDR models (right panels), computed for diffuse gas of density between 10 and 200 cm^{-3}. As mentioned above, we restrict our analysis to diffuse gas illuminated by the ambient ISRF, and have therefore removed all the data corresponding to lines of sight toward hot stars.

The TDR models predict column densities of CH$^+$ in good agreement with the observations for low densities ($n_H \leqslant 100$ cm^{-3}). This density limit corresponds to the observed average turbulent energy to which we scale our computations (Eq. (25)): if $\overline{\varepsilon}_{obs}$ was larger, this limit would be larger too. Most gratifying is the fact that this is achieved without producing an excess of CH. It is so because, in the vortex, CH is a product of CH$^+$ (its production is therefore enhanced by the turbulent dissipation, see Appendix C) but its destruction is also enhanced since it proceeds through endo-energetic reactions (CH + H, $-\Delta E/k = 2200$ K and CH + H$_2$, $-\Delta E/k = 1760$ K). Note that in panels (c, d), because of the assumed homogeneity of the gas (uniform A_V and n_H along the line of sight), the column densities computed in the TDR models are proportional to N_H, hence the straight lines.

Table 4. Same as Table 3.

	Parameters									
n_H	30 cm^{-3}					100 cm^{-3}				
A_V	0.4 mag					0.4 mag				
a	3 (-11) s^{-1}					3 (-11) s^{-1}				
	Physical properties									
$\overline{\Gamma}_{turb}$	8.5 (-24) erg cm^{-3} s^{-1}					6.2 (-23) erg cm^{-3} s^{-1}				
T_{amb}	79 K					42 K				
T_{max}	830 K					710 K				
τ_V	1250 yr					610 yr				
r_0	38 AU					20 AU				
$\mathcal{N}_{VA}$	246					19				
f_v	2.4 (-2)					3.2 (-3)				
	Chemical properties									
Species	$f_M(X)$ %	$f_{VA}(X)$ %	$f_{VR}(X)$ %	$N(X)$ cm^{-2}	$N(X)/N_H$	$f_M(X)$ %	$f_{VA}(X)$ %	$f_{VR}(X)$ %	$N(X)$ cm^{-2}	$N(X)/N_H$
H	100	0^a	0^a	2.0 (20)	1.1 (-01)	100	0^a	0^a	7.9 (19)	4.4 (-02)
H$_2$	100	0^a	0^a	8.0 (20)	4.4 (-01)	100	0^a	0^a	8.6 (20)	4.8 (-01)
H$_3^+$	77	6	17	5.9 (13)	3.3 (-08)	92	2	6	1.4 (13)	7.8 (-09)
C	19	56	25	1.3 (15)	7.2 (-07)	76	13	11	1.4 (15)	7.8 (-07)
CH	2	87	11	3.6 (13)	2.0 (-08)	20	66	14	1.5 (13)	8.3 (-09)
CH$^+$	0.2	96	4	1.3 (13)	7.2 (-09)	3	93	4	6.0 (11)	3.3 (-10)
C$_2$	0.3	57	43	4.2 (12)	2.3 (-09)	3	30	67	4.2 (12)	2.3 (-09)
C$_2$H	0.1	68	32	7.4 (12)	4.1 (-09)	0.4	52	47	1.0 (13)	5.6 (-09)
OH	47	24	29	8.4 (13)	4.7 (-08)	34	31	35	1.5 (13)	8.3 (-09)
H$_2$O	50	20	30	1.3 (13)	7.2 (-09)	39	27	34	2.4 (12)	1.3 (-09)
H$_3$O$^+$	20	46	34	9.9 (12)	5.5 (-09)	11	59	30	7.0 (11)	3.9 (-09)
CO	45	15	40	1.2 (14)	6.7 (-08)	35	11	54	9.1 (13)	5.1 (-08)
HCO$^+$	6	82	12	2.2 (12)	1.2 (-09)	3	84	13	4.9 (11)	2.7 (-10)
O$_2$	64	16	20	6.9 (10)	3.8 (-11)	52	19	29	4.4 (10)	2.4 (-11)
SH$^+$	0.02	97	3	1.7 (12)	9.4 (-10)	0.03	96	4	4.9 (11)	2.7 (-10)
CS	1	82	17	1.9 (10)	1.1 (-11)	9	61	30	3.0 (10)	1.7 (-11)
HCS$^+$	0.2	92	8	9.2 (09)	5.1 (-12)	1	86	13	6.1 (09)	3.4 (-12)
CN	2	67	31	8.8 (11)	4.9 (-10)	10	46	44	4.7 (11)	2.6 (-10)
HCN	1	84	15	1.0 (11)	5.6 (-11)	3	75	2	5.7 (10)	3.2 (-11)
HNC	2	87	11	2.7 (10)	1.5 (-11)	18	69	13	1.2 (10)	6.7 (-12)

^{a} Same as Table 3.

The dissipation of turbulent energy is also a plausible explanation for the excitation of the pure rotational levels of molecular hydrogen: the TDR models reproduce not only the CH$^+$ to H$_2^*(J = 4)$ column density ratio but also a significant fraction of the large dynamic range (2 orders of magnitude) over which the correlation is observed (Figs. 8e, f). We recall that all the column densities of species dominated by the warm chemistry are proportional to $\overline{\varepsilon}_{obs}$ and may be under- or over-estimated by about a factor of 10.

An encouraging result is also shown in Figs. 8g, h. Gry et al. (2002) and Lacour et al. (2005) found that the H$_2$ excitation diagrams obtained in the direction of stars later than B2 cannot be reproduced with the stellar UV excitation only. For comparison we display a PDR and a TDR model, both computed for $n_H = 100$ cm^{-3}, a value close to the optimal density found by Nehmé et al. (2008b) toward HD 102065.

The dependence of the TDR models on the density significantly differs from those of the PDR models. They share the same dependence of the chemistry on gas density but the TDR models have the additional dependence on density of the number of vortices and their size. The column density of CH$^+$ is therefore highly dependent on n_H (varies roughly as n_H^{-2}) while those of CH and H$_2^*(J \geqslant 3)$ are almost insensitive to the density in the range of parameters explored. Last, the turbulent rate of strain a has a weak effect: all the column densities decrease by less than a factor of 10 when a increases by a factor of 100.

6.2. Submillimeter and millimeter observations: absorption lines towards continuum sources

Conspicuous correlations have been observed in the diffuse ISM among the observed column densities of OH, H$_2$O, HCO$^+$, CO, C$_2$H, CN, HCN and HNC seen in absorption along lines of sight towards extragalactic radio sources or star forming regions. The column densities of several species appear to be linearly correlated. Some are tight correlations such as $N(OH)/N(HCO^+) = 27 \pm 7$ (Lucas & Liszt 1996), $N(CN)/N(HCN) = 6.8 \pm 1$, and $N(HNC)/N(HCN) = 0.21 \pm 0.05$ (Liszt & Lucas 2001) in the direction of extragalactic radio sources. Others are looser correlations, still linear, such as $N(H_2O)/N(HCO^+) \sim 6$ (Olofsson et al., submitted) and $N(H_2O)/N(OH) \sim 0.3$ (Neufeld et al. 2002) found in several velocity components towards galactic star forming regions. The column densities of CO and C$_2$H appear non-linearly correlated to those of HCO$^+$ (Liszt & Lucas 1998; Lucas & Liszt 2000). In all cases, these correlations are observed over a dynamic range of column densities as large as $30-100$.

To determine whether these large dynamic ranges correspond to actual variations of molecular relative abundances or
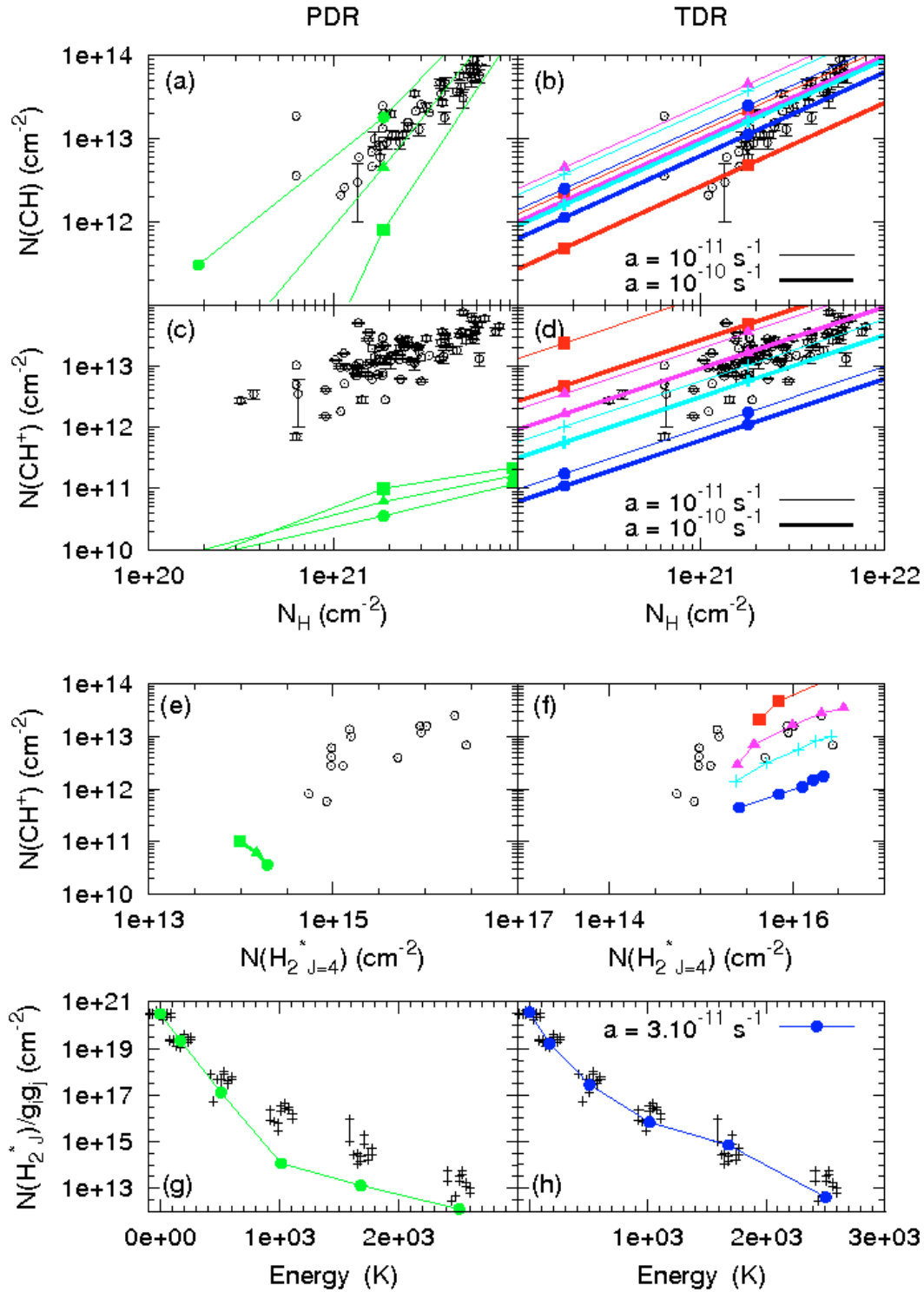
Fig. 8. Observations compared to PDR models (*left panels*) and to TDR models (*right panels*). Data (open circles) – CH column densities are from Crane et al. (1995) and Gredel (1997). CH$^+$ column densities are from Crane et al. (1995), Gredel (1997) and Weselak et al. (2008). H$_{2\ J=4}^*$ column densities are from Spitzer et al. (1974), Snow (1976, 1977), Frisch (1980), Frisch & Jura (1980) and Lambert & Danks (1986). The excitation diagrams of H$_2$ are from Gry et al. (2002) and Lacour et al. (2005). The data on panels **e**), **f**) and **g**), **h**) are scaled to $N_H = 1.8 \times 10^{21}$ cm^{-2} and $N(H_2) = 5 \times 10^{20}$ cm^{-2} respectively, and correspond to lines of sight toward stars of type later than B2. For clarity, on panels **g**), **h**), the points for a given level are slightly shifted on the abscissa. PDR and TDR models (filled symbols) – Computed for several densities: 10 (squares), 30 (triangles), 50 (crosses) and 100 cm^{-3} (circles). All the TDR models are computed for $A_V = 0.2$. The models of panels **e**), **f**) and **g**), **h**) have been scaled as the data. In panel **f**) the TDR models are computed for a varying along each curve between 10^{-11} (*top right*) and 10^{-9} s^{-1} (*bottom left*).

are due to a large range of column densities of gas sampled, we have estimated the total amount of gas $N_H = N(HI) + 2N(H_2)$ along the lines of sight used in our study, whenever it was possible. Using the $\lambda 21$ cm observations of HI (Du Puy et al. 1969;

Radhakrishnan et al. 1972; Lazareff 1975; Dickey et al. 1978) on the one side, and the measurement of the $\lambda 9$ cm line of CH and the remarkable correlation between CH and H_2 in the diffuse ISM (Liszt & Lucas 2002) on the other side, we estimated the total H column density for several lines of sight diplayed in Figs. 9 and 10. We found that most lines of sight sample about 1 mag of gas, with the exception of the upper point of panels (a, b) that corresponds to $2.5 \times 10^{21} < N_H < 3.6 \times 10^{21}$ cm^{-2} and the lowest for which $N_H = 6 \times 10^{20}$ cm^{-2}. The next 2 points both verify $N_H \geqslant 1.2 \times 10^{21}$ cm^{-2}. The dynamic range of $30-100$ observed on the column densities in Figs. 9 and 10 is therefore due in a small part to the amount of gas on the line of sight, and the actual dynamic range of observed relative abundances, $N(X)/N_H$, remains as large as about 10 along these diffuse lines of sight.

All these data are displayed in Figs. 9 and 10. The left panels show the predictions of several PDR models while the right panels display those of the TDR models for comparison (normalized to 1 magnitude of diffuse gas sampled on the line of sight). The calculations were made assuming a recombination rate of HCO$^+$ of $k = 2.4 \times 10^{-7}(T/300$ K$)^{-0.69}$ cm^{-3} s^{-1} (Ganguli 1988). This recombination rate being critical for some of the molecules presented here, we discuss the impact of this choice in Appendix A.

6.2.1. OH, H$_2$O and HCO$^+$

For these molecules, the PDR models predict linear correlations between their abundances, but they fail to reproduce the observed ratios and the observed dynamic range of absolute abundances.

The TDR models, without fine-tuning of the parameters, are consistent with the data over a broad range of gas densities 10 cm^{-3} $\leqslant n_H \leqslant$ 200 cm^{-3} and rates of strain 10^{-11} s^{-1} $\leqslant a \leqslant 10^{-10}$ s^{-1}. Better agreement is obtained for small values of the rate of strain, i.e. a chemistry dominated by ion-neutral drift heating. Not only are the abundance ratios correctly reproduced by the TDR models, but the dynamic ranges are also reproduced even with a single value of $\overline{\varepsilon}_{obs}$. Moreover these results are obtained without producing water abundances in excess of observed values. The models at high densities are consistent with the upper limit reported in HST-GHRS observations by Spaans et al. (1998).

6.2.2. C$_2$H and HCO$^+$

In the case of C$_2$H, we find that the observed column densities are reproduced by several models, something that the PDR models cannot even approach. The average abundance ratio $N(C_2H)/N(HCO^+) = 14.5 \pm 6.7$ (Lucas & Liszt 2000) is reproduced for almost the same models that match the observed column densities of OH and H$_2$O: 30 cm^{-3} $\leqslant n_H \leqslant$ 200 cm^{-3} and rates of strain 10^{-11} s^{-1} $\leqslant a \leqslant 10^{-10}$ s^{-1}.

6.2.3. CO and HCO$^+$

In the case of CO, the TDR models are closer to the observed column densities than the PDR model predictions, and again, high densities and low rates of strain are more favorable. In Appendix B we show, however, that if the energy dissipated in a vortex lifetime τ_V is reduced by a factor of 10 (i.e. the importance of the relaxation phase is increased by a factor of 10), the whole range of observed CO column densities is naturally reproduced for $n_H \geqslant 100$ cm^{-3} without significantly modifying the results regarding the other molecules.

The clumpiness and large fluctuations of density along the line of sight – often required to find an agreement between observed and predicted column densities in UV-driven chemical models (e.g. Black & Dalgarno 1977; Le Petit et al. 2006) – are not required here.

6.2.4. CN, HCN and HNC

The TDR models fail to reproduce the high column densities observed for CN, HCN and HNC, although the results are one to two orders of magnitude above the PDR models predictions. This discrepancy might be due to the nitrogen chemistry which involves neutral-neutral reactions whose rates are poorly known (Pineau des Forêts et al. 1990; Boger & Sternberg 2005).

6.3. The departure of carbon from ionization equilibrium

Figure 11 shows that the neutral carbon abundance predicted by the TDR models is higher by up to a factor of 10 than that of the PDR models where carbon is in ionization balance. This may be related to the finding of Fitzpatrick & Spitzer (1997) that the electron density inferred from C and C$^+$ is higher than those inferred from other pairs of ions and neutrals (Mg, S, Ca).

7. Discussion

7.1. The gas homogeneity

In our TDR models, the ambient chemistry is not treated with accurate UV radiative transfer. Instead, we assume that all the CNM on the line of sight has the same shielding from the ambient UV radiation field, no matter its density and column density. This takes into account the fractal structure of the CNM (Elmegreen et al. 2001) also found in the numerical simulations of Audit & Hennebelle (2005) and similar to that of edges of molecular clouds (Falgarone et al. 1991) and translucent molecular clouds (Stutzki et al. 1998). It also takes into account the fact that fragments that bear molecules are not isolated in space but are shielded from the ambient UV field by their neighbouring fragments (see Dobbs et al. 2008). This however does not have a major impact on our results for all the species that form predominantly in the warm chemistry, i.e. most of the species discussed here.

7.2. The assumption of isochoric evolution

During the vortex stage, the incompressibilty is reasonably justified. (1) Radially, the advection force is 3 to 10^3 times larger than the neutral thermal pressure gradients $\nabla_r (n_n k T_n)$ over the whole structure. Since it is also 10^2 to 10^3 times greater than the friction force F_{in} (see Sect. 2.3), $\nabla_r (n_n k T_n) \sim 1 - 30 F_{in}$. The ion thermal pressure gradients $\nabla_r (n_i k T_i) \sim 2 \times 10^{-4} \nabla_r (n_n k T_n)$ are consequently negligible compared to F_{in}. The assumption in Eq. (11), involved in the computation of the steady state, is therefore jusitified. (2) Along the z axis $\nabla_z (n_n k T_n)$ is smaller than the advection force as long as $a \geqslant 10^{-10}$ s^{-1}. For $a \leqslant 10^{-10}$ s^{-1} these terms are comparable. In this case, the axial expansion timescale is ~ 1000 yr, within a factor of 3 of the vortex lifetime (see Fig. 6).

During the relaxation phase, the thermal pressure gradients are dominant and therefore drive its dynamical evolution. According to the temperature gradients of Fig. 2 (panel c), the inner regions ($r \leqslant 0.5r_0$) should be compressed while the outer regions ($r \geqslant 1.5r_0$) should expand. The characteristic timescales
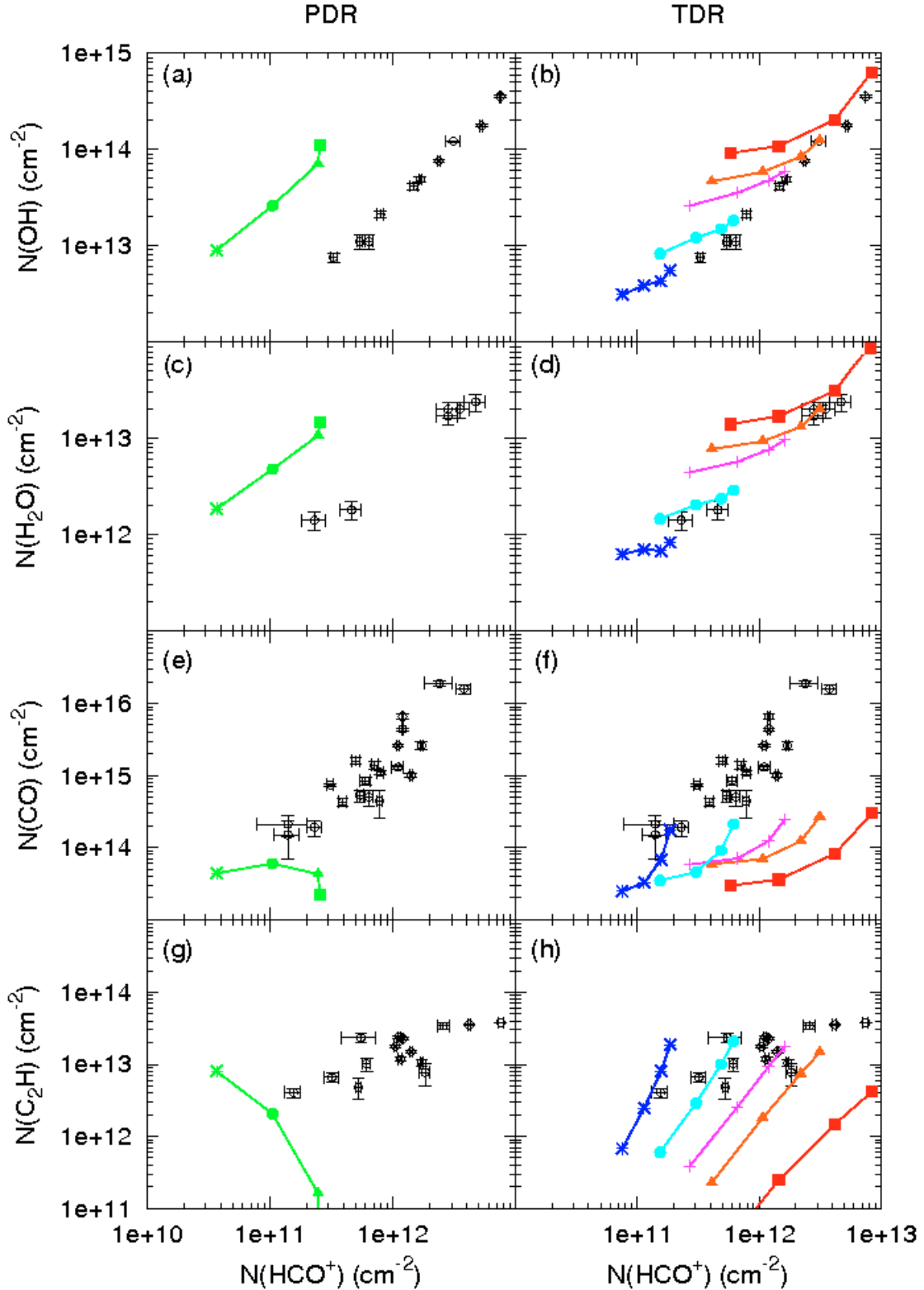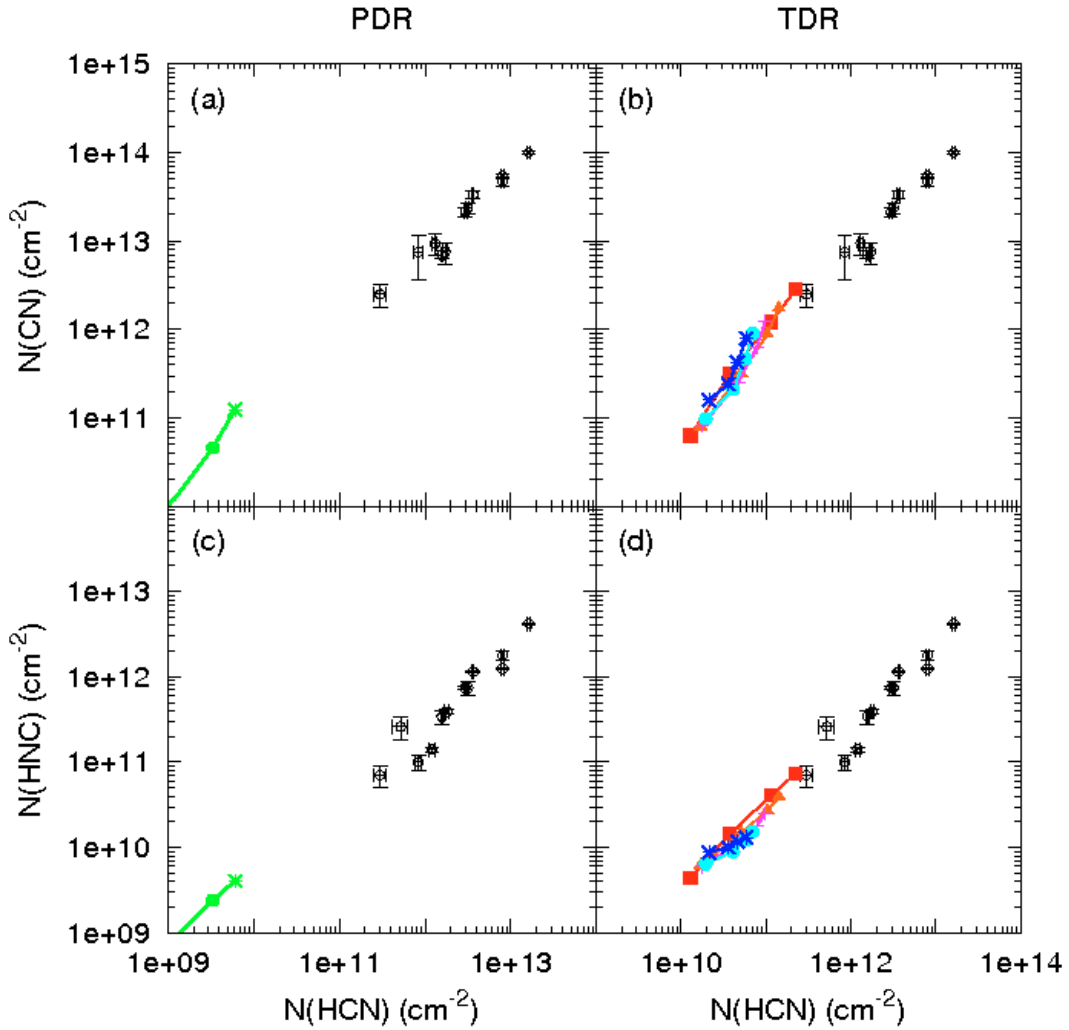
Fig. 9. Observations compared to PDR models (*left panels*) and to TDR models (*right panels*). Data (open circles) – the data of panels **a)**, **b)**, **c)**, **d)**, **e)**, **f)** and **g)**, **h)** are from Lucas & Liszt (1996), Olofsson et al. (submitted to A&A), Liszt & Lucas (1998) and Lucas & Liszt (2000) respectively. PDR and TDR models (filled symbols) – computed for several densities: 10 (squares), 30 (triangles), 50 (crosses), 100 (circles) and 200 (double crosses) cm^{-3}. All models are computed for $N_{\rm H} = 1.8 \times 10^{21}$ cm^{-2} and the HCO$^+$ recombination rate of Ganguli et al. (1988). The TDR models are computed for $A_{\rm V} = 0.4$ and a varying along each curve between 10^{-11} (*top right*) and 3×10^{-10} s^{-1} (*bottom left*).

associated with those motions are found to be short compared to the chemical timescales (see Sect. 4.3). However, an isochoric relaxation was assumed because the regions that are chemically the richest and have the largest contribution to the column densities are those where the thermal pressure gradients are the smallest ($0.5r_0 \leqslant r \leqslant 1.5r_0$).

Fig. 10. Observations compared to PDR models (*left panels*) and to TDR models (*right panels*). Data (open circles) – the data are from Liszt & Lucas (2001). PDR and TDR models (filled symbols) – same as Fig. 9.

7.3. Loosening the vortex framework

The vortex is a model that has the great and unique advantage of analytically coupling the large and small scales, but the knowledge we have of its lifetime is drawn from laboratory experiments only. This lifetime τ_V however plays an important role in the modelling of a diffuse line of sight: Eq. (23) shows that if a species is predominantly produced during the relaxation phase, its column density is proportional to $1/\tau_V$.

We have made the choice in Sect. 5.2.3 to infer τ_V from the total energy E dissipated in the vortex, under the constraint that τ_V remains larger than the vortex period. We show in Appendix B how the TDR model results are modified when E (and therefore τ_V) is ten times larger or smaller than the adopted value. As expected, the impact of E is greater for the molecules that have a long relaxation time. Figure B.1 shows that a small value of E leads to a better agreement with the available observations. This is shown for OH and CO but the same behavior is observed for CN, HCN and HNC. Such a result is in favour of very short bursts of turbulent dissipation, for which τ_V may become (at small a) shorter than the vortex period.

A non steady state model of a short-lived but intense velocity-shear may thus be more realistic and produce an equivalent chemical enrichment. This suggests that the vortex framework is not essential.

7.4. The chemistry

One source of uncertainties is undoubtedly linked to the chemistry itself. While the results are weakly dependent on the dynamic parameters a and n_H, a few reaction rates are critical. This is illustrated by Fig. A.1 that displays the predictions of the PDR and TDR models for a recent value (measured in the laboratory, Mitchell & Mitchell 2006) of the recombination rate of HCO^+.

The uncertainties on other chemical rates such as the recombination rate of $HCNH^+$ (Mitchell & Mitchell 2006) and the CN photodissociation rate (Kopp 1996), and neglected reactions (with negative ions for instance, see Dalgarno & MacCray 1973) might affect our modelling.

In this respect, a promising route would be to further link the observations of Sect. 6.1 and those of Sect. 6.2 by using the species that are detectable in both UV and radio domains: for instance CH, CN, OH and CO. These molecules would permit us to establish valuable correlations between CH^+ and the oxygen bearing species. It would also be a way to evaluate the column density of molecular hydrogen using two independent methods: the remarkable correlation between CH and H_2 (Liszt & Lucas 2002) and the less reliable correlation between CN and H_2 (Liszt & Lucas 2001).
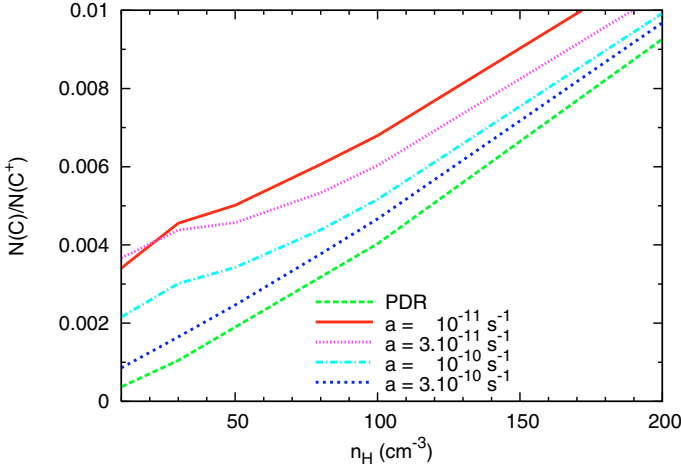
Fig. 11. Column densities ratio $N(C)/N(C^+)$ computed with the PDR and TDR codes, as functions of the density n_H.

8. Conclusions and perspectives

We have built TDR models of diffuse gas in which the gas temperature and chemistry are driven by small-scale bursts of turbulence dissipation. We use the framework of a modified Burgers vortex to analytically couple the large scales of the ambient turbulence to the small scales where dissipation actually occurs, and to compute the ion-neutral drift generated by the large neutral accelerations in the vortex. The resulting timescales are short and comparable to those of chemical evolution, which necessitates a non-equilibrium thermal and chemical approach.

The main feature of these TDR models is that, for the first time, we quantify the coexistence on a random line of sight across the medium, of a number of vortices in a stage of active dissipation with gas in thermal and chemical relaxation, after the end of the dissipation burst. We also constrain the number of dissipative structures on a line of sight by the average turbulent energy available in the local ISM and its transfer rate in the cascade. The key parameter is the turbulent rate of strain a due to the ambient turbulence.

We find that these bursts of dissipation, short-lived and localized, fill at most a few percent of a random line of sight but have a measurable impact on the molecular abundances in the diffuse medium. For a broad range of rates of strain and densities, the TDR models reproduce the CH$^+$ column densities observed in the diffuse medium and their correlation with highly excited H$_2$. They do so without producing an excess of CH.

As a natural consequence, they reproduce the correct abundance ratios of HCO$^+$/OH and HCO$^+$/H$_2$O, and the dynamic range of about one order of magnitude over which they are observed. Larger C$_2$H and CO abundances than found in other types of models, are additional outcomes of the TDR models that compare reasonably well with the observed values and their relation to the HCO$^+$ abundances. Those results are found for a broad range of physical parameters, with rates of strain in the range 10^{-11} s$^{-1} \leqslant a \leqslant 10^{-10}$ s^{-1}.

We find that neutral carbon exceeds the abundance expected at ionization equilibrium, in agreement with fine-structure line observations. The abundances and column densities computed for CN, HCN and HNC are one order of magnitude above PDR predictions and close to the observed values, although a discrepancy still exists.

The comparison with observed column densities favors chemical enrichment dominated by ion-neutral friction, involving shear structures of radius ~100 AU or more. It also favors short dissipation bursts. Most of the species are then produced during the relaxation phase. In this case, their line profile loses the dynamic signatures of the vortex. The fact that some species are formed in the active phases and some others in the relaxation phases might explain the discrepancy among the physical gas parameters inferred from different species along similar lines of sight.

It is foreseeable that the vortex framework and the assumption of an isochoric relaxation will have to be superseded by numerical simulations to:

(1) compute the decoupling of magnetic field and neutrals in the intense small-scale velocity-shears generated by intermittency, with boundary conditions imposed by large scale turbulence,
(2) take into account the effect of the field on the velocity shears,
(3) accurately involve all the pressure gradients (thermal and magnetic) in the relaxation phase, and
(4) take advantge of the huge amount of information contained in the shape of the line profiles. The difficulty will remain to couple the large and small scales, over at least 5 orders of magnitude, that is critical to satisfy the energy requirements of the TDR models and is currently beyond the numerical capabilities.

Appendix A: The recombination of HCO$^+$

One critical reaction rate of our work is the recombination of HCO$^+$ which determines the equilibrium between the oxygen bearing molecules (OH, CO, H$_2$O, ...). The associated rate k has varied over more than an order of magnitude during the last 30 years among various experiments.

Adams et al. ([1982](#)) and Amano ([1990](#)) performed measurements of k (studying respectively a flowing and a stationary afterglow plasma) in a temperature range of 100 K $\leqslant T \leqslant$ 300 K and found respectively 1.1×10^{-7} cm^3 s^{-1} at 300 K and 3.1×10^{-7} cm^3 s^{-1} at 273 K. In 1988 Ganguli et al. (stationary afterglow plasma) explored the high energy domain 293 K $\leqslant T \leqslant$ 5500 K and obtained a scaling law:

$$k = 2.4 \times 10^{-7} \times (T/300 \text{ K})^{-0.69} \text{ cm}^3 \text{ s}^{-1}. \tag{A.1}$$

In approximatively the same range of energy (but with the merged beam measurement technique) Le Padellec et al. ([1997](#)) obtained

$$k = 1.7 \times 10^{-7} (T/300 \text{ K})^{-1.2} \text{ cm}^3 \text{ s}^{-1}. \tag{A.2}$$

Later the same group (Mitchell & Mitchell [2006](#)) revised their previous value by taking into account the exploration of the low energy domain ($\leqslant$0.01 eV). They found:

$$k = 0.7 \times 10^{-7} \times (T/300 \text{ K})^{-0.5} \text{ cm}^3 \text{ s}^{-1}. \tag{A.3}$$

More recently Korolov et al. (in press, flowing aftergow plasma) performed measurements in the range 150 K $\leqslant T \leqslant$ 270 K. They obtained results in good agreement with those of Le Padellec et al. ([1997](#)), this is to say a steep dependence on the temperature:

$$k = 2.0 \times 10^{-7} \times (T/300 \text{ K})^{-1.3} \text{ cm}^3 \text{ s}^{-1}. \tag{A.4}$$
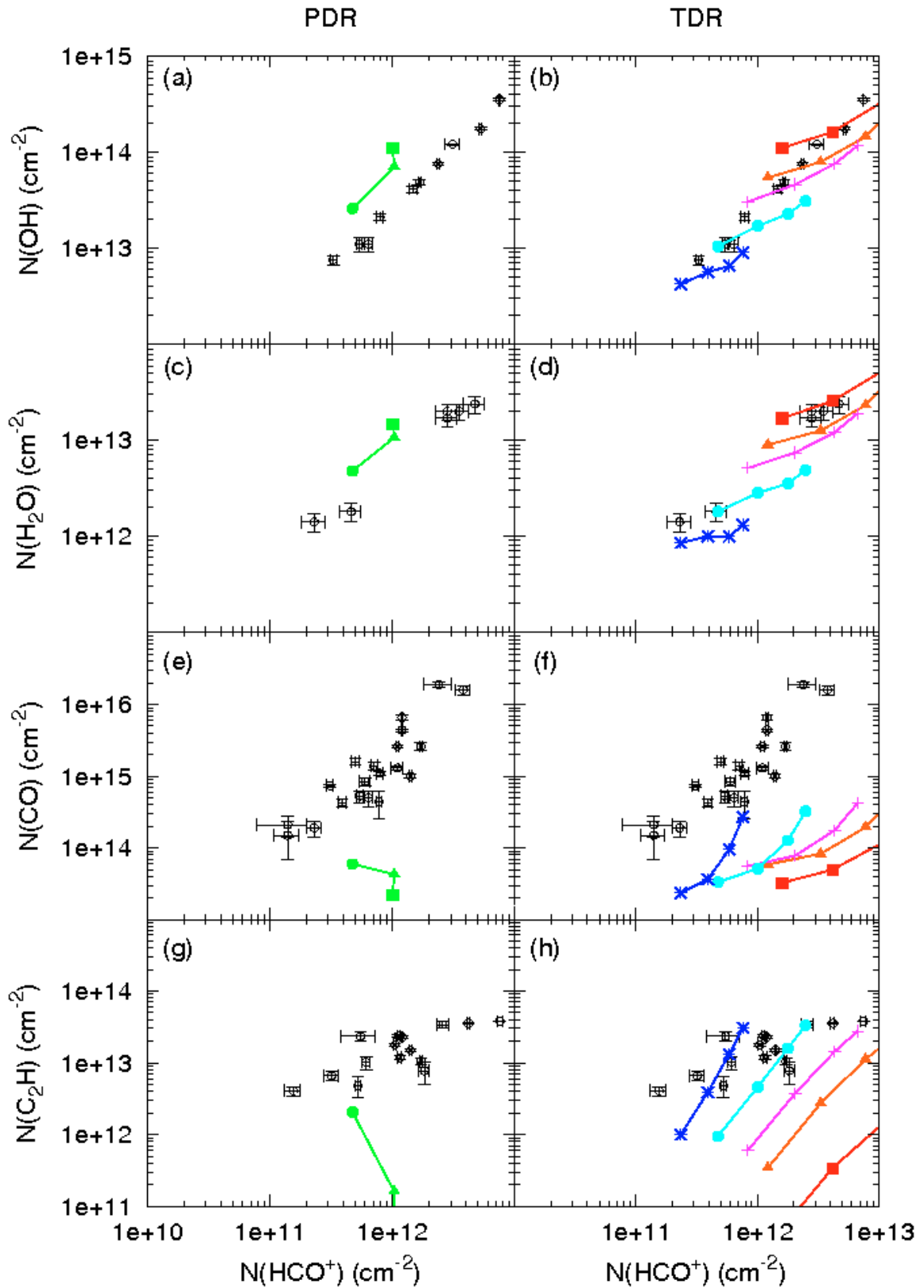
Fig. A.1. Observations compared to PDR models (*left panels*) and to TDR models (*right panels*). Data (open circles) – same as Fig. 9. PDR and TDR models (filled symbols) – same as Fig. 9 except for the recombination rate of HCO$^+$ chosen to be $0.7 \times 10^{-7}(T/300 \text{ K})^{-0.5}$ cm^3 s^{-1} (Mitchell & Mitchell 2006).

Figure A.1 displays the results we obtain with the TDR and PDR models assuming the rate of Mitchell & Mitchell (2006) which is the smallest yet found. In comparison Fig. 9 was obtained assuming the rate of Ganguli et al. (1988) which is one of the highest and is usually adopted in other chemical networks (UMIST database; OSU database).
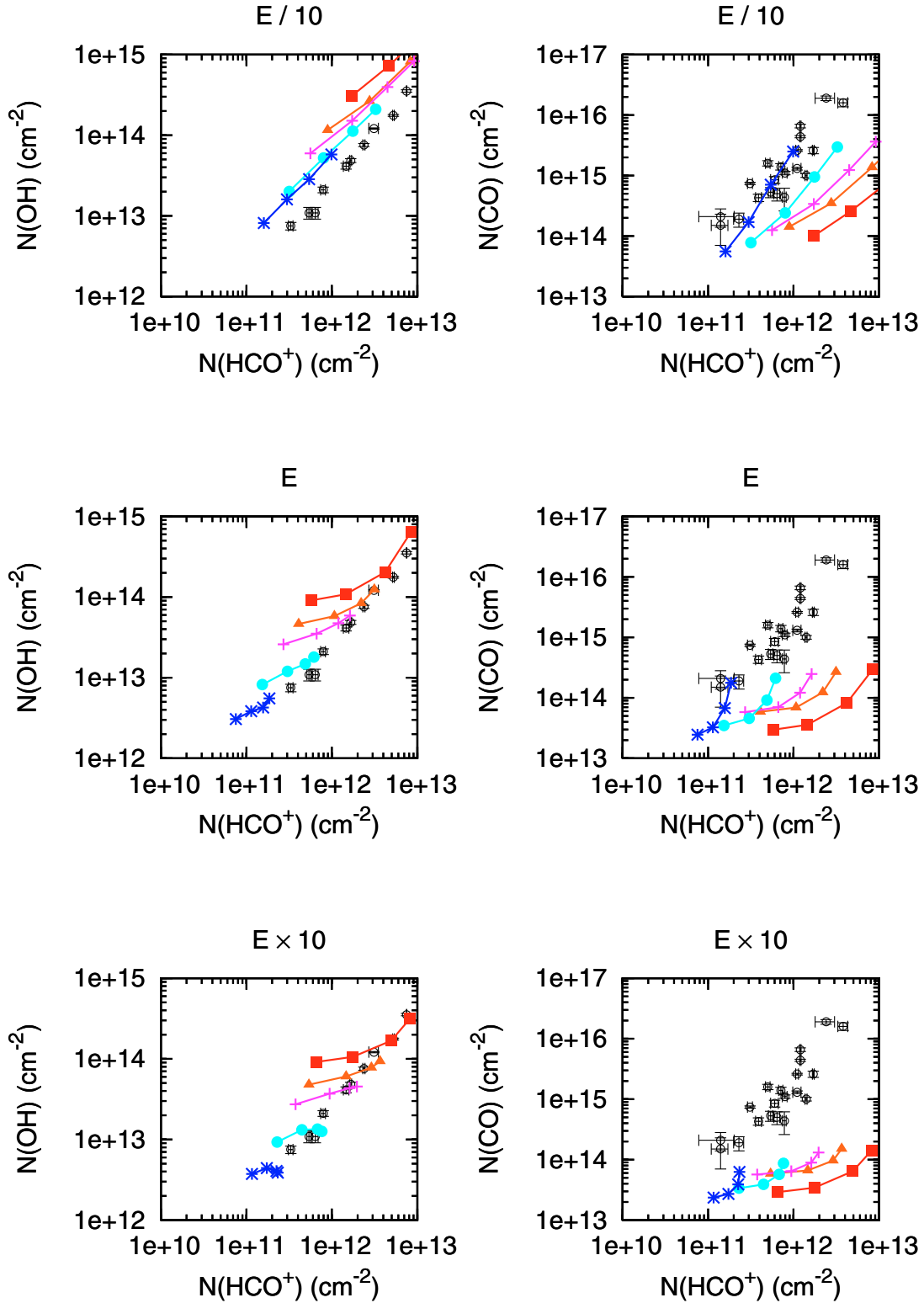
Fig. B.1. Observations compared to the TDR models. The data are from Lucas & Liszt (1996) and Liszt & Lucas (1998). The TDR models are scaled to $N_H = 1.8 \times 10^{21}$ cm^{-2} and are computed for several values of the total energy E dissipated by a vortex: from 0.1 (*top panels*) to 10 times (*bottom panels*) that of the reference model. The symbols are the same as in Fig. 9.

Appendix B: Influence of the total energy E dissipated per vortex

Figure B.1 illustrates the effect on the column densities of OH, CO and HCO$^+$ of varying the energy dissipated in the vortex E by two orders of magnitude.

Figure B.1 suggests that small values of E lead to better agreement with the observations. Smaller amounts of dissipated energy, in our framework, means shorter vortex lifetimes, that accordingly give a larger relative importance to the relaxation phase (Eq. (23)). In the models displayed on the top panels, the lifetime is such that the relaxation phase dominates the
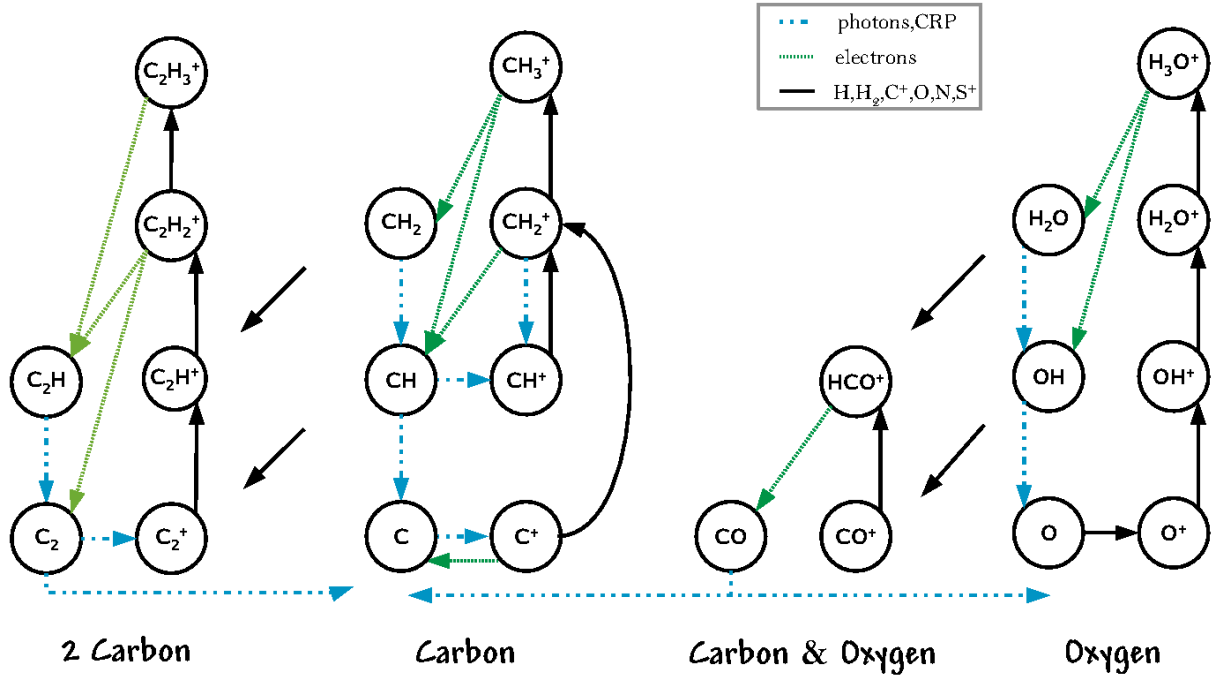
Fig. C.1. Chemical network of a UV-dominated chemistry: $n_H = 30$ cm^{-3} and $A_V = 0.4$. This figure is simplified: for each species only the dominant reaction of production and the dominant reaction of destruction are displayed.
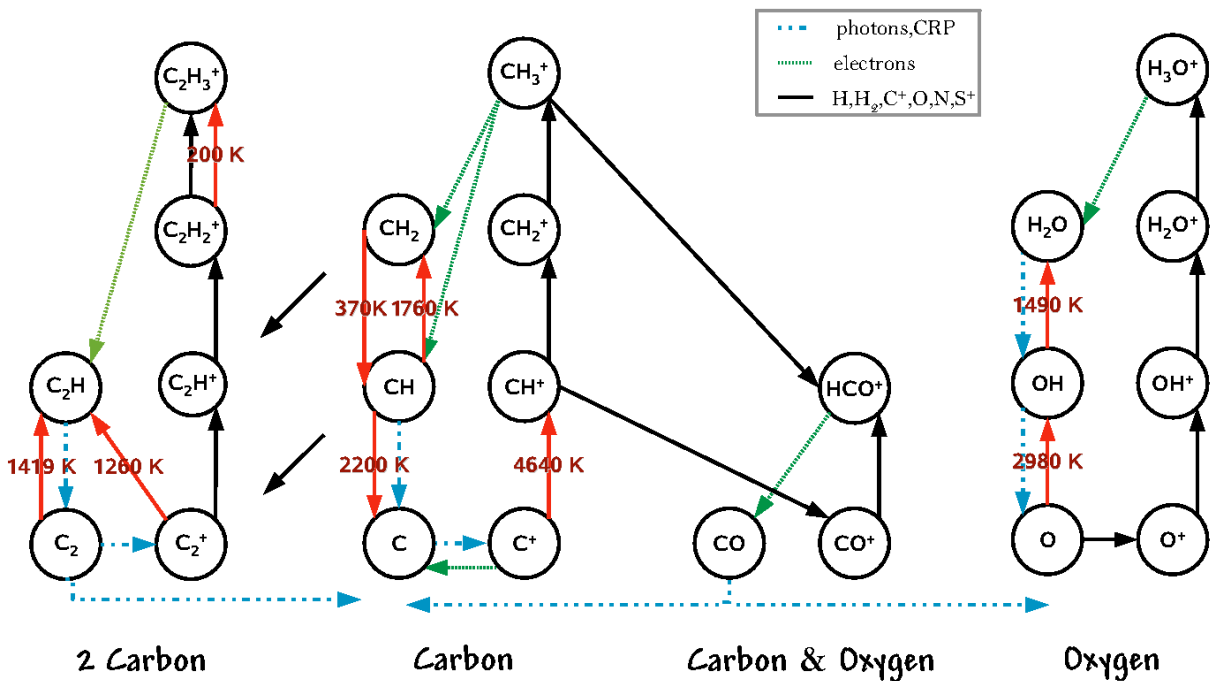

Fig. C.2. Same as Fig. C.1 for a turbulence-dominated chemistry: $n_H = 30$ cm^{-3}, $A_V = 0.4$, $a = 3 \times 10^{-11}$ s^{-1} at a radius $r = r_0$. The red arrows show the endoenergetic reactions with the energy involved.

production of almost all the species we are interested in, namely CH, C$_2$H, OH, H$_2$O, HCO$^+$, CO, CN, HCN and HNC.

Appendix C: UV-dominated versus turbulence-dominated chemical networks

Figures C.1 and C.2 display the main production and destruction routes of the molecules of interest in the ambient UV-dominated

diffuse medium and in the vortex for the reference TDR model at a radius $r = r_0$ respectively.

These figures are simplified: *only* the dominant reaction of production and the dominant reaction of destruction of the species are shown. For example one would expect the reaction O + H$_3^+$ → OH$^+$ + H$_2$ to be displayed in Fig. C.1. But in the model presented here, the efficiency of this reaction on the production of OH$^+$ is only 12%, while the efficiency of O$^+$ + H$_2$ → OH$^+$ + H is 86%. Therefore it does not appear on the diagram.

References

Adams, N. G., Smith, D., & Alge, E. 1982, J. Chem. Phys., 81, 4
Amano, T. 1990, J. Chem. Phys., 92, 11
Anselmet, F., Antonia, R. A., & Danaila, L. 2001, Planet. Space. Sci., 49, 1177
Audit, E., & Hennebelle, P. 2005, A&A, 433, 1
Belin, F., Maurer, J., Tabeling, P., & Willaime, H. 1996, J. Phys., 6, 573
Black, J. H., & Dalgarno, A. 1977, ApJS, 34, 405
Black, J. H., Dalgarno, A., & Oppenheimer, M. 1975, ApJ, 199, 633
Boger, G. I., & Sternberg, A. 2005, ApJ, 632, 302
Brandenburg, A., Jennings, R. L., Nordlund, A., et al. 1996, J. Fluid Mech., 306, 325
Brown, P. N., Byrne, G. D., & Hindmarsh, A. C. 1989, J. Sci. Stat. Comput., 10, 1038
Crane, P., Lambert, D. L., & Sheffer, Y. 1995, ApJS, 99, 107
Crovisier, J. 1981, A&A, 94, 162
Dalgarno, A. 2006, PNAS, 103, 33
Dalgarno, A., & McCray, R. A. 1973, ApJ, 181, 95
Dickey, J. M., Salpeter, E. E., & Terzian, Y. 1978, ApJS, 36, 77
Dobbs, C., Glover, S., Clark, P., & Klessen, R. 2008, MNRAS, 389, 1097
Douady, S., Couder, Y., & Brachet, M. E. 1991, Phys. Rev. Lett., 67, 8
Draine, B. 1978, ApJS, 36, 59
Draine, B. T., & Katz, N. 1986, ApJ, 310, 392
Du Puy, D., Schmitt, J., McClure, R., van den Bergh, S., & Racine, R. 1969, ApJ, 156, L135
Elmegreen, B. G., Kim, S., & Staveley-Smith, L. 2001, ApJ, 58, 749
Falgarone, E. 1998, in Starbursts: Trigger, Nature and Evolution, ed. B. Guiderdoni, & A. Kembhavi (EPS Sciences)
Falgarone, E. 1999, in Interstellar Turbulence, ed. J. Franco, & A. Carraminana (Cambridge University Press)
Falgarone, E., Philipps, T. G., & Walker, C. K. 1991, ApJ, 378, 186
Falgarone, E., Lis, D. C., Phillips, T. G., et al. 1994, ApJ, 436, 728
Falgarone, E., Pineau des Forêts, G., & Roueff, E. 1995, A&A, 300, 870
Falgarone, E., Verstraete, L., Pineau des Forêts, G., & Hily-Blant, P. 2005, A&A, 433, 997
Falgarone, E., Pineau des Forêts, G., Hily-Blant, P., & Schilke, P. 2006, A&A, 452, 511
Fitzpatrick, E. L., & Spitzer, L. 1997, ApJ, 475, 623
Flower, D. R., & Pineau des Forêts, G. 1995, MNRAS, 275, 1049
Flower, D. R., & Pineau des Forêts, G. 1998, MNRAS, 297, 1182
Frisch, P. C. 1980, ApJ, 241, 697
Frisch, P. C., & Jura, M. 1980, ApJ, 242, 560
Ganguli, B., Biondi, M. A., Johnsen, R., & Dulaney, J. L. 1988, Phys. Rev., 37, 7
Gredel, R. 1997, A&A, 320, 929
Gredel, R., Van Dishoeck, E. F., & Black, J. H. 1993, A&A, 269, 477
Gry, C., Boulanger, F., Nehmé, C., et al. 2002, A&A, 391, 675
Haud, U., & Kalberla, P. M. W. 2007, A&A, 466, 555
Hartmann, L., & Burton, W. B. 1997, Atlas of Galactic Neutral Hydrogen (Cambridge University Press)
Heiles, C., & Troland, T. H. 2003, ApJ, 586, 1067
Heiles, C., & Troland, T. H. 2005, ApJ, 624, 773
Hily-Blant, P., Falgarone, E., & Pety, J. 2008, A&A, 481, 367
Jimenez, J. 1997, Euromech Colloquium, 384
Joncas, G., Boulanger, F., & Dewdney, P. E. 1992, ApJ, 397, 165
Joulain, K., Falgarone, E., Pineau des Forêts, G., & Flower, D. 1998, A&A, 340, 241
Kay, G. W. C., & Laby, T. H. 1966, Tables of physical and chemical constants (Londres: Longmans)
Kopp, M. 1996, Ph.D. Thesis, Université Paris 7
Kritsuk, A. G., Norman, M. L., Padoan, P., & Wagner, R. 2007, ApJ, 665, 416
Lacour, S., Ziskin, V., Hébrard, G., et al. 2005, A&A, 627, 251
Lambert, D. L., & Danks, A. C. 1986, ApJ, 303, 401

Lambert, D. L., Sheffer, Y., & Crane, P. 1990, ApJ, 359, L19
Lazareff, B. 1975, A&A, 42, 25
Le Padellec, A., Sheehan, C., Talbi, D., & Mitchell, J. B. A. 1997, J. Phys. B, 30, 319
Le Petit, F., Nehmé, C., Le Bourlot, J., & Roueff, E. 2006, ApJS, 160, 506
Lesaffre, P., Gerin, M., & Hennebelle, P. 2007, A&A, 469, 949
Liszt, H. S., & Lucas, R. 1998, A&A, 339, 561
Liszt, H., & Lucas, R. 2001, A&A, 370, 576
Liszt, H., & Lucas, R. 2002, A&A, 391, 693
Liszt, H., Lucas, R., & Pety, J. 2006, A&A, 448, 253
Lucas, R., & Liszt, H. 1996, A&A, 307, 237
Lucas, R., & Liszt, H. 2000, A&A, 358, 1069
Lucas, R., & Liszt, H. 2002, A&A, 384, 1054
Martin-Zaïdi, C., Deleuil, M., Le Bourlot, J., et al. 2005, A&A, 484, 225
Mininni, P. D., Alexakis, A., & Pouquet, A. 2006a, Phys. Rev., 74, 1
Mininni, P. D., Pouquet, A. G., & Montgomery, D. C. 2006b, Phys. Rev. Lett., 97, 24
Mitchell, A. I., & Mitchell, J. B. A. 2006, Phys. Rep., 430, 277
Miville-Deschênes, M. A., Joncas, G., Falgarone, E., & Boulanger, F. 2003, A&A, 411, 109
Moffatt, H. K., Kida, S., & Ohkitani, K. 1994, J. Fluid Mech., 259, 241
Moisy, F., & Jimenez, J. 2004, J. Fluid Mech., 513, 111
Monchick, L., & Schaefer, J. 1980, J. Chem. Phys., 73, 61, 53
Nehmé, C., Gry, C., Boulanger, F., et al. 2008a, A&A, 483, 471
Nehmé, C., Le Bourlot, J., Boulanger, F., Pineau des Forêts, G., & Gry, C. 2008b, A&A, 483, 485
Nagaoka, K., Okamoto, A., Yoshimura, S., Kono, M., & Tanaka, M. Y. 2002, Phys. Rev. Lett., 89, 7
Neufeld, D. A., Kaufman, M. J., Goldsmith, P. F., Hollenbach, D. J., & Plume, R. 2002, ApJ, 580, 278
Nolan, D. S., & Farrell, B. F. 1999, J. Atmos. Sci., 56, 2908
Pan, L., & Padoan, P. 2008, ApJ, in press
Pan, K., Federman, S. R., Cunha, K., et al. 2004, ApJS, 151, 313
Pan, K., Federman, S. R., Sheffer, Y., & Andersson, B. G. 2005, ApJ, 633, 936
Pavlovski, G., Smith, M. D., & Mac Low, M.-M. 2006, MNRAS, 368, 943
Pety, J., & Falgarone, E. 2000, A&A, 356, 279
Pineau des Forêts, G., Flower, D. R., Hartquist, T. W., & Dalgarno, A. 1986, MNRAS, 220, 801
Pineau des Forêts, G., Roueff, E., & Flower, D. R. 1990, MNRAS, 244, 668
Porter, D. H., Pouquet, A., & Woodward, P. R. 1992, Phys. Rev. Lett., 68, 21
Porter, D. H., Pouquet, A., & Woodward, P. R. 1994, Phys. Fluids, 6, 2133
Radhakrishnan, V., Murray, J. D., Lockhart, P., & Whittle, P. J. 1972, ApJS, 24, 15
Ritchey, A. M., Martinez, M., Pan, K., et al. 2006, ApJ, 649, 788
Savage, B. D., Drake, J. F., Budich, W., & Bohlin, R. C. 1977, ApJ, 216, 291
Sheffer, Y., Rogers, M., Federman, S. R., et al. 2008, ApJ, 687, 1075
Shull, J. M., & Beckwith, S. 1982, AARA, 20, 163
Snow, T. P. 1976, ApJ, 204, 759
Snow, T. P. 1977, ApJ, 216, 724
Snow, T. P., & McCall, B. J. 2006, ARA&A, 44, 367
Sonnentrucker, P., Friedman, S. D., Welty, D. E., et al. 2003, ApJ, 596, 350
Spaans, M., Neufeld, D., Lepp, S., Melnick, G. J., & Stauffer, J. 1998, ApJ, 503, 780
Spitzer, L. 1978, Physical processes in the interstellar medium (New York: J. Wiley & Sons)
Spitzer, L., Drake, J. F., Morton, D. C., et al. 1973, ApJ, 181, L116
Spitzer, L., Cochran, W. D., & Hirshfeld, A. 1974, ApJS, 28, 373
Sternberg, A., & Dalgarno, A. 1975, ApJS, 99, 565
Stutzki, J., Bensch, F., Heithausen, A., et al. 1998, A&A, 336, 697
Weselak, T., Galazutdinov, G., Musaev, F., & Krelowski, J. 2008, A&A, 479, 149
White, R. E. 1984, ApJ, 284, 695
White, R. E. 2003, ApJS, 148, 487